Meteoritics & Planetary Science 34, 829–848 (1999)

A study of the minor element concentrations of spinels from two type B calcium-aluminum-rich inclusions: An investigation into potential formation conditions of calcium-aluminum-rich inclusions

HAROLD C. CONNOLLY, JR.* AND D. S. BURNETT

Division of Geological and Planetary Sciences, California Institute of Technology, Mail Code 100-23, Pasadena, California 91125, USA
*Correspondence author's e-mail address: vorlon@gps.caltech.edu

(Received 1998 May 29; accepted in revised form 1999 July 1)

Abstract–We have conducted an electron microprobe study of minor element distributions among spinels from two type B1 calcium-aluminum-rich inclusions (CAIs): Allende TS-23 and Leoville 3537-2. We show that by maintaining the petrologic context (edge, middle, and center of the inclusion plus their host silicate phase), four populations of spinels are resolvable based on their minor element contents. One population resides within the edge area (mainly mantle melilite) and is characterized by the highest V contents. Unlike Leoville 3537-2, many edge grains from Allende TS-23 also have high-Fe contents (up to 4.0 wt%) and low-Cr values. Based on their V and Ti concentrations (which is positively correlated), middle and center grains define a trend that is divided into three populations: spinels enclosed by melilite, fassaite, and anorthite. The overall range in Ti concentration based on fractional crystallization should be much less than a factor of 2; however, the observed range is considerably larger. The minor element contents of these grains are interpreted as recording alteration, primary fractional crystallization, and a complex igneous history that may involve remelting and recrystallization. From our data, Allende TS-23 has experienced more alteration than Leoville 3537-2, which is consistent with previous petrologic studies of silicates within these objects; yet both objects have likely been remelted (at least one additional melting event, possibly two, postdating the initial formation of these CAIs). By invoking a remelting history, the large range in Ti concentrations and the different populations of spinels can be explained. Although our data suggest that more than one generation of spinels exist within these objects, we are unable to establish any population of relic spinel grains that predate the initial melting event.

INTRODUCTION

Type B calcium-aluminum-rich inclusions (CAIs) are rocks found within carbonaceous chondrites. They are the oldest known igneous objects (~4.5 Ga; *e.g.*, Chen and Wasserburg, 1981) and can contain evidence of short-lived radionuclide, such as ^{26}Al. The precursors of these objects were likely the first solid planetary materials to condense from a gas of solar composition (Grossman, 1972; Yoneda and Grossman, 1995). Through the study of these earliest of solar system materials, it is possible to reconstruct specific information concerning their formation environment and the processes that operated to produce and alter them.

Originating within our protoplanetary nebula as free-floating objects (Stolper, 1982), many type B CAIs have not survived billions of years as completely pristine objects. They are commonly altered to varying degrees with veins of secondary minerals. The location and timing of the postcrystallization event(s) that distorted their igneously derived geochemical signatures is unknown. Furthermore, it has been suggested that some type B CAIs experienced multiple cycles of heating, melting, and crystallization (Davis and MacPherson, 1996; El Goresy *et al.*, 1985; MacPherson *et al.*, 1988; MacPherson and Davis, 1993; Meeker, 1995; Paque, 1990), although understanding of this recycling is limited.

The mineralogy of type B CAIs is dominated by spinel + melilite + anorthite + clinopyroxene (Ti-rich member known as fassaite). Most scientific studies of these solar system materials have concentrated on understanding their formation or alteration by exploring silicates, compositional relationships between silicates and the bulk, and any deviation of silicate geochemistry from predicted values (*e.g.*, trace element partitioning, *etc.*). Although studies of silicates has helped to illuminate the history of type B CAIs, systematic investigation into the minor element chemistry of spinel ($MgAl_2O_4$), thus unlocking the potentially unique memories that the spinel may have recorded, has not been performed.

For type B CAIs, spinel is the liquidus phase and thus should be the least sensitive to any petrologic complications (*e.g.*, disequilibrium crystallization) that might occur during the later stages of crystallization. In addition, if relic grains exist in CAIs (*e.g.*, Paque, 1990), the most likely candidate is spinel. The maximum temperature experienced by type B CAIs has been experimentally constrained to be within the spinel + liquid field; thus if multiple generations of melting occurred, spinels from earlier generations may have survived. One potentially important method to identifying relic spinels or any alteration experienced by spinels postcrystallization is to establish their minor element concentrations and deviation of such abundances from fractional crystallization predictions. Herein we present new data on a study designed to explore the igneous and alteration histories of CAIs through the minor element distribution within and among spinels from two type B1 inclusions.

EXPERIMENTAL TECHNIQUES

Spinels from two well-characterized (MacPherson *et al.*, 1984, 1988; Caillet *et al.*, 1993) type B1 inclusions were analyzed: Allende TS-23 (Fig. 1) and Leoville 3537-2 (Fig. 2). We selected areas from both inclusions based solely on position within the inclusion. For Leoville 3537-2, two areas are located within the mantle melilite, which we term edge area (excluding the Wark–Lovering rim), and two areas each were selected within the middle and center part of the object. A total of seven areas within Allende TS-23 were selected, three within the mantle melilite or edge areas (excluding the Wark–Lovering rim), and two areas each from the middle and center part of the inclusion. We did not investigate the

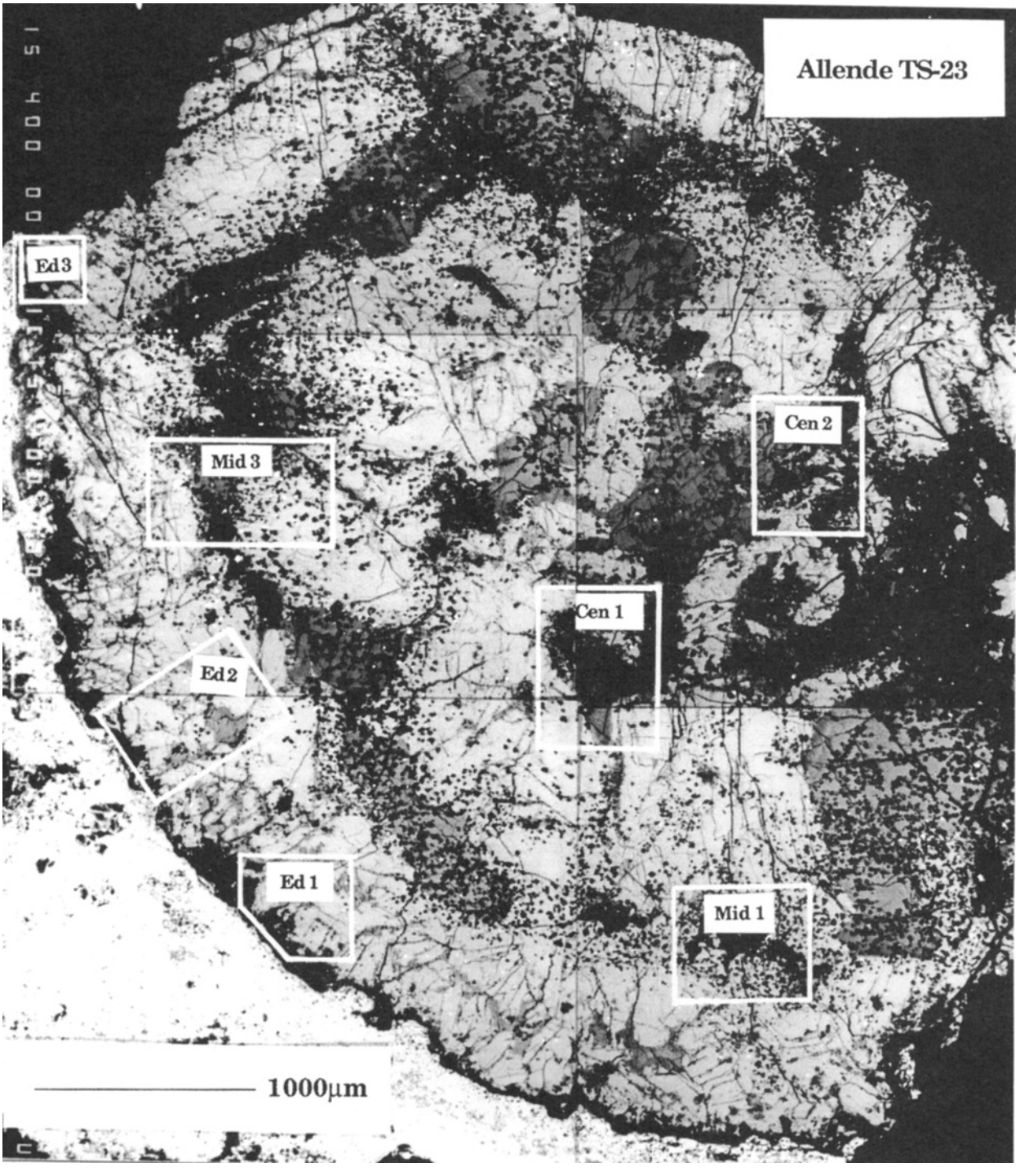

FIG. 1. Backscatter electron composite image of Allende TS-23. The areas used in our study are outlined in white and marked either Ed (edge), Mid (middle), or Cen (center). This section has been described in some detail by MacPherson *et al.* (1988) and Beckett (1986).

Wark–Lovering rims because these almost certainly represent a secondary event. Within each area (*e.g.*, Fig. 3), a random selection of all spinels present were analyzed, for a total of 118 spinels from Leoville 3537-2 and 68 from Allende TS-23 (Tables 1 and 2, representing only acceptable analyses). The petrographic context of each spinel grain was carefully documented. Attention was given to recording the condition (*e.g.*, the presence of cracks, inclusions, *etc.*) of the spinels, their crystal form, the type of host silicate phases, the position of the spinels relative to any altered silicates or veins of alteration, and any major cracks that propagate within the inclusion. We also analyzed the host silicate phases in each area to provide a more complete petrologic context for our interpretations (Tables 3 and 4).

Analyses and backscattered electron (BSE) imaging were carried out on the JEOL 733 five-spectrometer electron microprobe at Caltech. For spinels (all $MgAl_2O_4$ *sensu stricto*), major (Mg and

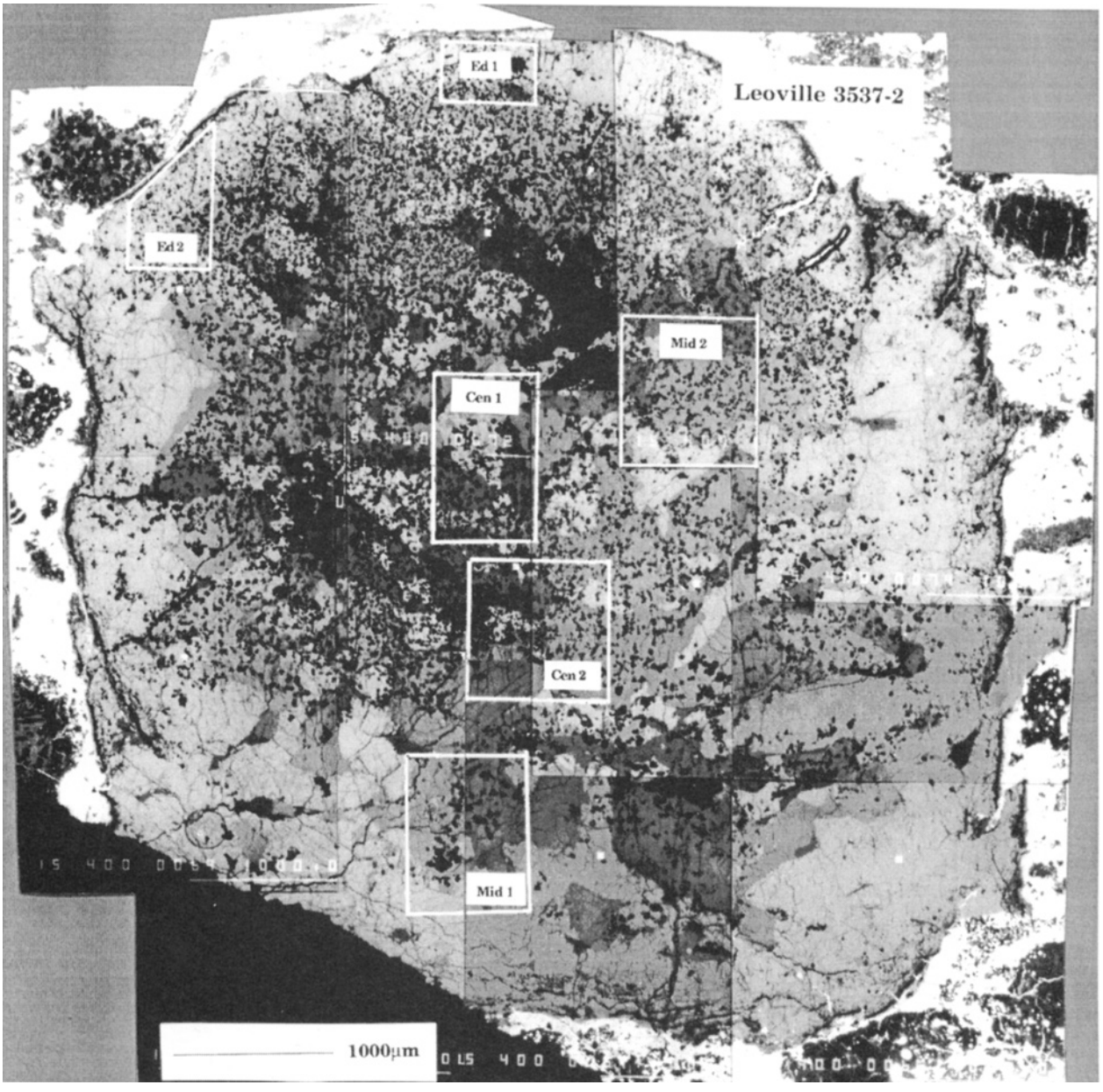

FIG. 2. Backscatter electron composite image of Leoville 3537-2. The areas used in our study are outlined in white and marked either Ed (edge), Mid (middle), or Cen (center). This object has been described in some detail by Calliet *et al.* (1993).

Al) and minor elements (Si, Ca, Ti, Cr, Mn, Fe, Zn, V) were analyzed with wavelength-dispersive (WDS) analysis, operating at an accelerating voltage of 15kV with a beam current as measured in the Faraday cup of 40 nA for major and 400 nA for minor elements. Counting times were 40 s for major elements and 120 s for minor elements. Silicate compositions (Mg, Al, Si, Ca, Ti, Cr, Mn, Fe, and V) were determined using WDS analysis operating at an accelerating voltage of 15kV with a beam current as measured in the Faraday cup of 40 nA and counting times of 40 s. Corrections for TiK_β interference with VK_α and VK_β interference with CrK_α were applied to all analyses. Standards were well-characterized natural and synthetic minerals. Because the grain size of spinels were small (rarely above 25 μm), the contribution from continuum secondary fluorescence is an issue, permitting only one analysis (within the center) per spinel grain. Data reduction was based on CITZAF1, version 3.04 (Armstrong, 1995); and only data with counting statistics errors of <30% were included. Although analyzed, Mn and Zn were below detection limits of 100 and 170 ppmw, respectively, for all analyses and will not be discussed below. Silicon and Ca were included in our element list for spinel analyses mainly as an indicator to ensure that analyses were of spinels only, not overlapping onto silicate.

RESULTS

Overall Petrology of Inclusions and Their Spinels

Leoville 3537-2 was described by Caillet *et al.* (1993). Our study is on the same thin section described in this paper. The object is a typical type B1 CAI, although its mantle melilite is not as well

TABLE 1. Electron microprobe analyses (reported as parts per million, ppmw) of the minor element content of spinels ($MgAl_2O_4$, designated Sp) from six different areas within the type B1, CAI Leoville 3537-2.*

Sample #	Host	Ti (ppm)	Cr (ppm)	Fe (ppm)	V (ppm)
Ed 1					
Sp1	Mel	1650 ± 74	1046 ± 45	334 ± 57	3578 ± 122
Sp2	Mel	1433 ± 64	844 ± 36	392 ± 67	3680 ± 125
Sp3	Mel	1640 ± 74	1050 ± 45	335 ± 57	3461 ± 118
Sp5	Mel	1578 ± 71	1040 ± 45	364 ± 62	3336 ± 113
Sp6	Mel	1512 ± 68	1055 ± 45	380 ± 65	3325 ± 113
Sp8	Mel	1906 ± 86	1090 ± 47	265 ± 45	3570 ± 121
Sp9†	Mel	1702 ± 77	1095 ± 47	276 ± 47	3364 ± 114
Sp10	Mel	1571 ± 71	1138 ± 49	585 ± 100	3438 ± 117
Sp11‡	Mel	1895 ± 85	1123 ± 48	239 ± 41	3522 ± 120
Sp12†	Mel	1741 ± 78	1117 ± 48	248 ± 42	3365 ± 114
Sp16	Mel	1601 ± 72	1197 ± 51	244 ± 42	3612 ± 123
Sp17	Mel	2236 ± 101	1231 ± 53	257 ± 44	3009 ± 102
Sp18	Mel	1417 ± 64	1162 ± 50	431 ± 73	2932 ± 100
Sp19	Mel	2050 ± 92	1114 ± 48	281 ± 48	3390 ± 115
Ed 2					
Sp1	Mel	2060 ± 93	1061 ± 46	240 ± 41	3198 ± 109
Sp2†	Mel	2014 ± 91	1114 ± 48	249 ± 42	3395 ± 115
Sp4	Mel	2127 ± 96	1120 ± 48	231 ± 39	3335 ± 113
Sp5	Mel	1863 ± 84	1138 ± 49	235 ± 40	3317 ± 113
Sp8†	Mel	1715 ± 77	919 ± 40	2424 ± 412	3476 ± 118
Sp9	Mel	1934 ± 87	1083 ± 47	277 ± 47	3593 ± 122
Sp10†	Mel	1966 ± 88	1095 ± 47	660 ± 112	3384 ± 115
Sp12†	Mel	1125 ± 51	810 ± 35	715 ± 122	3346 ± 114
Sp13†	Mel	1680 ± 76	998 ± 43	270 ± 46	3476 ± 118
Sp14†	Mel	2247 ± 101	1129 ± 49	273 ± 46	3426 ± 116
Sp15	Mel	2181 ± 98	1115 ± 48	214 ± 36	3398 ± 116
Sp16†	Mel	1630 ± 73	1112 ± 48	304 ± 52	3193 ± 109
Sp17	Fs	3711 ± 167	1178 ± 51	286 ± 49	2733 ± 93
Sp18†	Fs	3386 ± 152	1161 ± 50	514 ± 87	2853 ± 97
Sp20	Fs	3547 ± 160	1148 ± 49	247 ± 42	3115 ± 106
Sp21†	Fs	4285 ± 193	1132 ± 49	253 ± 43	3095 ± 105
Mid 1					
Sp1†	Fs	2867 ± 129	1272 ± 55	272 ± 46	2966 ± 101
Sp2	Fs	3242 ± 146	1267 ± 54	349 ± 59	3232 ± 110
Sp3	Fs	2723 ± 123	1192 ± 51	336 ± 57	2818 ± 96
Sp4	Fs	3649 ± 164	1162 ± 50	320 ± 54	2820 ± 96
Sp5	Fs	3363 ± 151	1103 ± 47	297 ± 51	3028 ± 103
Sp6	Fs	3345 ± 151	1089 ± 47	330 ± 56	3233 ± 110
Sp8	Fs	3310 ± 149	1095 ± 47	235 ± 40	2977 ± 101
Sp9†	Fs	3289 ± 148	1113 ± 48	286 ± 49	3000 ± 102
Sp10	Fs	3658 ± 165	1138 ± 49	440 ± 75	3221 ± 110
Sp11	Fs	3395 ± 153	1178 ± 51	316 ± 54	2953 ± 100
Sp12†	Fs	3127 ± 141	1089 ± 47	772 ± 131	3186 ± 108
Sp13	Fs	3623 ± 163	1168 ± 50	268 ± 46	2931 ± 100
Sp14	Fs	3185 ± 143	1119 ± 48	255 ± 43	2863 ± 97
Sp15	Fs	2882 ± 130	1099 ± 47	386 ± 66	2578 ± 88
Sp16	Fs	2648 ± 119	1151 ± 49	360 ± 61	2570 ± 87
Sp17	Mel	1365 ± 61	1664 ± 72	336 ± 57	1616 ± 55
Sp18	Mel	1581 ± 71	1211 ± 52	262 ± 44	3181 ± 108
Sp19	Fs	3514 ± 158	1126 ± 48	268 ± 46	3242 ± 110
Mid 2					
Sp2	Fs	1918 ± 86	1193 ± 51	678 ± 115	2003 ± 68
Sp3	Fs	3454 ± 155	1134 ± 49	265 ± 45	2777 ± 94
Sp4	Fs	3418 ± 154	1138 ± 49	221 ± 38	2868 ± 97
Sp5	Fs	3480 ± 157	1108 ± 48	243 ± 41	2959 ± 101
Sp7†	Fs	2235 ± 101	1206 ± 52	279 ± 47	2073 ± 70
Sp8†	Mel	1047 ± 47	1243 ± 53	280 ± 48	1752 ± 60
Sp9	Mel	1313 ± 59	1265 ± 54	476 ± 81	2178 ± 74
Sp10	Mel	1671 ± 75	1211 ± 52	251 ± 43	2327 ± 79
Sp11	Mel	1611 ± 73	1270 ± 55	294 ± 50	2202 ± 75
Sp12	Mel	1552 ± 70	1279 ± 55	278 ± 47	2164 ± 74
Sp13	Mel	1499 ± 67	1266 ± 54	324 ± 55	2108 ± 72
Sp14†	Mel	1654 ± 74	1164 ± 50	267 ± 45	2101 ± 71
Sp15	Mel	1439 ± 65	1215 ± 52	254 ± 43	1887 ± 64
Sp17	Mel	1412 ± 64	1216 ± 52	223 ± 38	2039 ± 69
Sp18	Mel	1474 ± 66	1157 ± 50	266 ± 45	2034 ± 69

TABLE 1. *Continued.*

Sample #	Host	Ti (ppm)	Cr (ppm)	Fe (ppm)	V (ppm)
Mid 2 *(continued)*					
Sp19	Mel	1144 ± 51	1263 ± 54	339 ± 58	1829 ± 62
Sp20	Fs	2680 ± 121	1145 ± 49	243 ± 41	2395 ± 81
Sp21	An	1072 ± 48	1185 ± 51	240 ± 41	1907 ± 65
Sp22	An	2388 ± 107	1200 ± 52	220 ± 37	2439 ± 83
Sp23	An	1582 ± 71	1232 ± 53	316 ± 54	1993 ± 68
Sp25†	An	1502 ± 68	1216 ± 52	444 ± 76	1962 ± 67
Sp26	An	1342 ± 60	1196 ± 51	472 ± 80	2390 ± 81
Sp27	An	1747 ± 79	1203 ± 52	379 ± 64	2612 ± 89
Sp28	An	2020 ± 91	1170 ± 50	293 ± 50	2650 ± 90
Sp32†	An	1786 ± 80	1208 ± 52	336 ± 57	2729 ± 93
Sp34†	Mel	1218 ± 55	1206 ± 52	417 ± 71	2207 ± 75
Cen 1					
Sp1	An	1431 ± 64	1246 ± 54	338 ± 57	2320 ± 79
Sp2†	Mel	962 ± 43	1179 ± 51	277 ± 47	1891 ± 64
Sp3†	Fs	1273 ± 57	1361 ± 59	346 ± 59	1815 ± 62
Sp5‡	Fs	1504 ± 68	1269 ± 55	440 ± 75	1818 ± 62
Sp7†,‡	Mel	1189 ± 54	1205 ± 52	238 ± 40	2038 ± 69
Sp8†	An	1794 ± 81	1178 ± 51	257 ± 44	2739 ± 93
Sp9	An	2605 ± 117	1214 ± 52	248 ± 42	2761 ± 94
Sp10	An	2002 ± 90	1236 ± 53	284 ± 48	2650 ± 90
Sp11†	Mel	932 ± 42	1306 ± 56	453 ± 77	2082 ± 71
Sp12	An	1285 ± 58	1174 ± 50	261 ± 44	2383 ± 81
Sp13	An	2661 ± 120	1160 ± 50	255 ± 43	2518 ± 86
Sp14†	An	1482 ± 67	1170 ± 50	256 ± 44	2421 ± 82
Sp15†	Fs	2580 ± 116	1332 ± 57	349 ± 59	2176 ± 74
Sp16	Mel	925 ± 42	1223 ± 53	339 ± 58	1773 ± 60
Cen 2					
Sp1	An	1610 ± 92	1224 ± 51	334 ± 59	1920 ± 63
Sp2	An	1784 ± 102	1300 ± 55	230 ± 41	2194 ± 72
Sp3	An	1706 ± 97	1278 ± 54	251 ± 44	1993 ± 66
Sp4	An	1562 ± 89	1289 ± 54	230 ± 41	2318 ± 76
Sp5	An	1847 ± 105	1165 ± 49	240 ± 43	2564 ± 85
Sp6	An	1761 ± 100	1223 ± 51	262 ± 46	2297 ± 76
Sp7	An	2309 ± 132	1240 ± 52	270 ± 48	2559 ± 84
Sp8	An	1850 ± 105	1201 ± 50	275 ± 49	2396 ± 79
Sp9	An	1247 ± 71	1194 ± 50	270 ± 48	2261 ± 75
Sp10†,‡	Mel	709 ± 40	1267 ± 53	325 ± 57	1634 ± 54
Sp12	Fs	1301 ± 74	1249 ± 52	374 ± 66	1652 ± 54
Sp13	An	1118 ± 64	1255 ± 53	254 ± 45	2002 ± 66
Sp14	Mel	1389 ± 79	1261 ± 53	293 ± 52	1905 ± 63
Sp15†	Mel	881 ± 50	1304 ± 55	386 ± 68	1648 ± 54
Sp16	Fs	2306 ± 131	1255 ± 53	307 ± 54	2108 ± 70
Sp18	Fs	1950 ± 111	1254 ± 53	302 ± 53	2033 ± 67
Sp19†	Fs	3020 ± 172	1173 ± 49	248 ± 44	2576 ± 85
Sp20	Fs	3170 ± 181	1217 ± 51	243 ± 43	2510 ± 83
Sp21†,‡	Fs	1529 ± 87	1184 ± 50	284 ± 50	2238 ± 74
Sp22†	Fs	1301 ± 74	1258 ± 53	253 ± 45	1847 ± 61
Sp23	Fs	1456 ± 83	1286 ± 54	339 ± 60	1746 ± 58
Sp25	Mel	1668 ± 95	1196 ± 50	236 ± 42	2522 ± 83
Sp26	Fs	1761 ± 100	1341 ± 56	334 ± 59	1569 ± 52
Sp28†	Fs	3061 ± 174	1186 ± 50	305 ± 54	2557 ± 84
Sp29	Fs	2708 ± 154	1235 ± 52	338 ± 60	2380 ± 79
Sp30†	Fs	3431 ± 196	1159 ± 49	278 ± 49	2777 ± 92
Sp32	Mel	741 ± 42	1375 ± 58	451 ± 80	1459 ± 48
Sp33†	Mel	619 ± 35	1335 ± 56	774 ± 137	1508 ± 50
Sp34†	Mel	1204 ± 69	1235 ± 52	266 ± 47	2159 ± 71

Notes: Mel = melilite, Fs = fassaite, and An = anorthite.

*The six areas were divided up based on their geographic location within the object, Edge (Ed), Middle (Mid), and Center (Cen). The silicate host phases enclosing each spinel are also reported (under Host). All data points below each highlighted area name (*i.e.*, Ed1) are located only within that area.

†Indicates that the designated spinel grain contains a crack of unknown origin that general y propagates into the surrounding host silicate phase.

‡Indicates that the designated spinel grain is located within an area (<100 μm) of either a melilite alteration zone, which was determined qualitatively by texture and EDS measurements, or brittle deformation area determined by texture (*i.e.*, broken angular fragments of pyroxene).

TABLE 2. Electron microprobe analyses (reported as parts per million, ppmw) of the minor element content of spinels ($MgAl_2O_4$, designated Sp) from seven different areas within the type B1, CAI Allende TS-23.*

Sample #	Host	Ti (ppm)	Cr (ppm)	Fe (ppm)	V (ppm)
Ed 1					
Sp1†,‡	Mel	2474 ± 37	1108 ± 17	466 ± 9	2288 ± 25
Sp2‡	Mel	1880 ± 28	763 ± 11	509 ± 10	2358 ± 26
Sp3	Mel	1460 ± 22	625 ± 9	17660 ± 336	2337 ± 26
Sp4‡	Mel	1618 ± 24	650 ± 10	10152 ± 193	2408 ± 26
Sp5†,‡	Mel	1804 ± 27	648 ± 10	19100 ± 363	2355 ± 26
Sp6†,‡	Mel	1823 ± 27	677 ± 10	8644 ± 165	2038 ± 22
Sp7‡	Mel	1792 ± 27	892 ± 13	896 ± 17	2507 ± 28
Ed 2					
Sp1†,‡	Mel	2238 ± 34	1966 ± 37	1415 ± 20	2123 ± 30
Sp3†,‡	Mel	2194 ± 33	1836 ± 35	305 ± 4	1863 ± 20
Sp7‡	Mel	1915 ± 29	1558 ± 30	4107 ± 57	1808 ± 20
Ed 3					
Sp1†,‡	Mel	1567 ± 23	600 ± 11	21904 ± 307	2769 ± 30
Sp2†,‡	Mel	1808 ± 27	579 ± 11	44011 ± 616	2669 ± 29
Sp4‡	Mel	1735 ± 26	658 ± 12	33128 ± 464	2750 ± 30
Sp9†	Mel	2115 ± 32	1298 ± 25	1644 ± 20	2581 ± 28
Mid 1					
Sp1†	An	1474 ± 22	1495 ± 28	1779 ± 25	1473 ± 16
Sp2†	An	1318 ± 20	1521 ± 29	546 ± 8	1432 ± 16
Sp4†	An	1130 ± 17	1459 ± 28	352 ± 5	1371 ± 15
Sp7	Mel	1623 ± 24	1739 ± 33	11041 ± 155	1504 ± 17
Sp8‡	Mel	1538 ± 23	1776 ± 34	6653 ± 93	1377 ± 15
Sp9†	Mel	1417 ± 21	1693 ± 32	5501 ± 77	1426 ± 16
Sp10†,‡	An	1392 ± 21	1930 ± 37	9093 ± 127	1581 ± 17
Sp13†,‡	Mel	1271 ± 19	1650 ± 31	436 ± 6	1248 ± 14
Sp14†,‡	Mel	1550 ± 23	1619 ± 31	1829 ± 26	1493 ± 16
Sp15†	Mel	1793 ± 27	1504 ± 29	2501 ± 35	1788 ± 20
Sp16‡	Mel	1498 ± 22	1510 ± 29	1645 ± 23	1541 ± 17
Sp17†,‡	Mel	1366 ± 20	1522 ± 29	444 ± 6	1403 ± 15
Sp18†,‡	Mel	1380 ± 21	1700 ± 32	1525 ± 21	1213 ± 13
Sp19‡	An	1357 ± 20	1677 ± 32	3286 ± 46	1290 ± 14
Sp20†,‡	Mel	1394 ± 21	1667 ± 32	1106 ± 15	1357 ± 15
Sp21‡	Mel	1487 ± 22	1676 ± 32	7017 ± 98	1368 ± 15
Mid 3					
Sp1†,‡	Mel	1413 ± 21	2013 ± 38	2226 ± 31	1474 ± 16
Sp2†,‡	Mel	1381 ± 21	1962 ± 37	6059 ± 85	1723 ± 19
Sp3†,‡	Mel	1641 ± 25	1672 ± 32	1047 ± 15	1741 ± 19
Sp4†,‡	Mel	1533 ± 23	1692 ± 32	751 ± 11	1592 ± 18
Sp5†,‡	Mel	1520 ± 23	1742 ± 33	1016 ± 14	1525 ± 17
Sp9	Fs	2197 ± 33	1519 ± 29	5976 ± 84	1413 ± 16
Sp10†	Fs	2301 ± 35	1404 ± 27	635 ± 9	1576 ± 17
Sp11†	An	1802 ± 27	1536 ± 29	771 ± 11	1436 ± 16
Sp12†	An	1957 ± 29	1509 ± 29	1799 ± 25	1408 ± 15
Sp13†	Fs	1323 ± 20	1627 ± 31	5914 ± 83	1184 ± 13
Sp14	Fs	1734 ± 26	1546 ± 29	5914 ± 83	1216 ± 13
Sp15†	An	1515 ± 23	1537 ± 29	1216 ± 17	1318 ± 14
Cen 1					
Sp1†	Fs	2041 ± 31	1389 ± 26	1034 ± 14	1197 ± 13
Sp2†	Fs	2060 ± 31	1374 ± 26	1265 ± 18	1186 ± 13
Sp3	Fs	2461 ± 37	1361 ± 26	906 ± 13	1414 ± 16
Sp4	Fs	2655 ± 40	1304 ± 25	526 ± 7	1381 ± 15
Sp5†	Fs	1910 ± 29	1773 ± 34	1911 ± 27	1256 ± 14
Sp6†	Fs	1998 ± 30	1546 ± 29	703 ± 10	1430 ± 16
Sp7†,‡	Mel	1065 ± 16	1894 ± 36	2416 ± 34	947 ± 10
Sp8†,‡	Mel	1225 ± 18	1940 ± 37	708 ± 10	1082 ± 12
Sp9†,‡	Mel	1083 ± 16	1836 ± 35	480 ± 7	1097 ± 12
Sp10†,‡	Mel	1054 ± 16	1951 ± 37	294 ± 4	928 ± 10
Sp12	Mel	1557 ± 0	1773 ± 34	506 ± 7	1385 ± 15
Sp14†,‡	Mel	1121 ± 17	1862 ± 35	4673 ± 65	1076 ± 12
Sp15†	Mel	1205 ± 18	1861 ± 35	509 ± 7	1111 ± 12
Sp17‡	Mel	1135 ± 17	1915 ± 36	1032 ± 14	1047 ± 12

TABLE 2. *Continued.*

Sample #	Host	Ti (ppm)	Cr (ppm)	Fe (ppm)	V (ppm)
Cen 2					
Sp1‡	Fs	1650 ± 25	1528 ± 23	4720 ± 66	1203 ± 13
Sp2†,‡	Fs	1919 ± 29	1416 ± 21	1674 ± 0	1242 ± 14
Sp3‡	Fs	1670 ± 25	1544 ± 0	2663 ± 37	1100 ± 12
Sp6	Fs	2563 ± 38	1358 ± 20	590 ± 8	1787 ± 20
Sp8†,‡	Mel	1388 ± 21	1478 ± 22	2286 ± 32	1219 ± 13
Sp10	Fs	2253 ± 34	1366 ± 20	612 ± 9	1419 ± 16
Sp11‡	Fs	1346 ± 20	1669 ± 25	2305 ± 32	1153 ± 13
Sp12†,‡	Mel	1401 ± 21	1684 ± 25	1747 ± 24	1347 ± 15
Sp13†,‡	Mel	1413 ± 21	1676 ± 25	613 ± 9	1295 ± 14
Sp14†,‡	Mel	1420 ± 21	1630 ± 24	912 ± 13	1367 ± 15
Sp15‡	Mel	1365 ± 20	1574 ± 24	438 ± 6	1361 ± 15

Notes: Mel = melilite, Fs = fassaite, and An = anorthite.
*The seven areas are divided up based on their geographic location within the object, Edge (Ed), Middle (Mid), and Center (Cen). The silicate host phases enclosing each spinel are also reported (under Host). All data points listed below each highlighted area name (*i.e.*, Ed1) are located only within that designated area.
†Indicates that the designated spinel grains contain a crack of unknown origin that generally propagates into the surrounding host silicate phase.
‡Indicates that the designated spinel grain is located within an area of melilite alteration that was determined qualitatively by texture and EDS measurements.

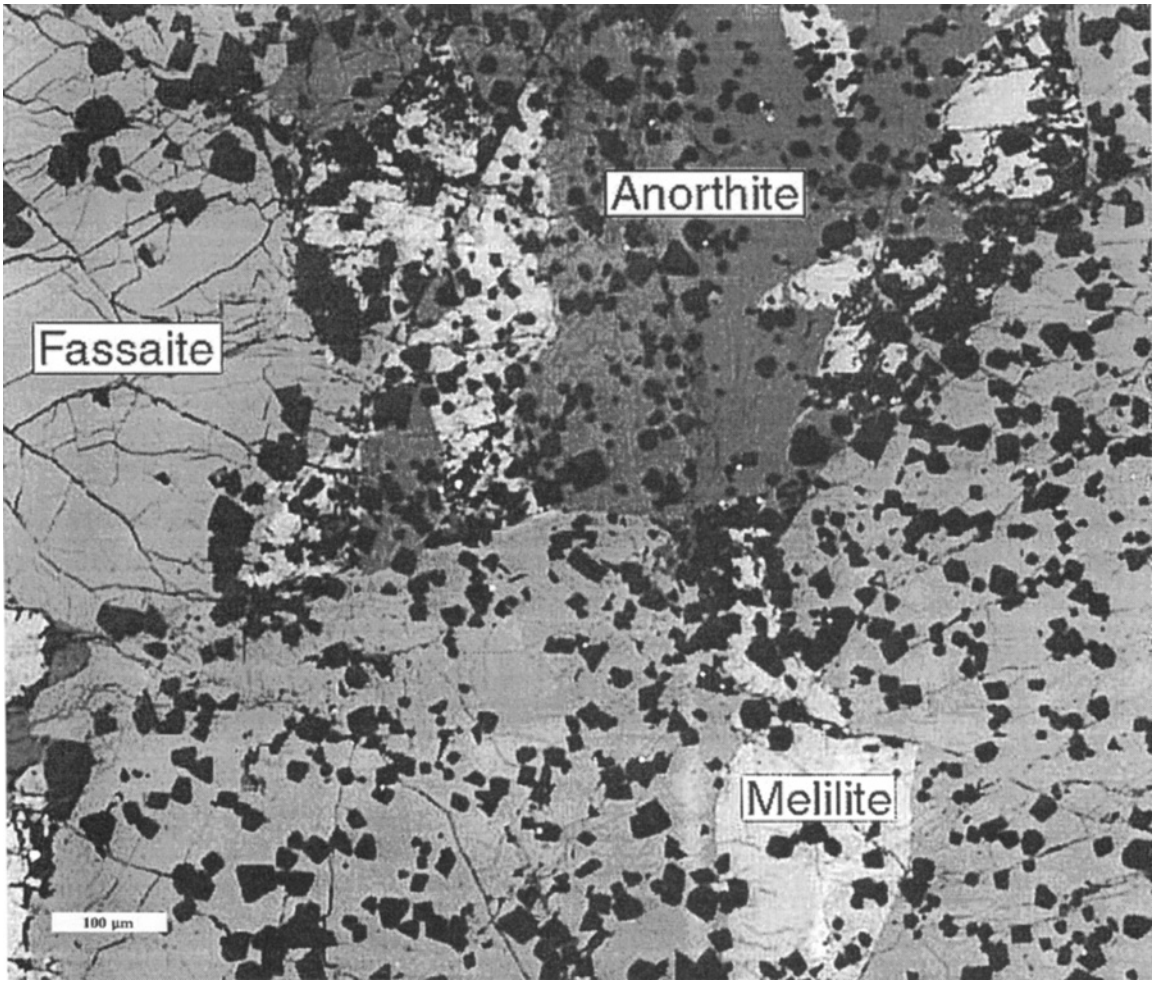

FIG. 3. Backscatter electron image of a representative area of study, Center 2, from Leoville 3537-2. The small dark grains are spinel. In order of increasing reflectivity, the other phases are anorthite, fassaite, and melilite. The size of the image is 750 × 900 μm. This is a typical texture for the core regions of type B CAIs.

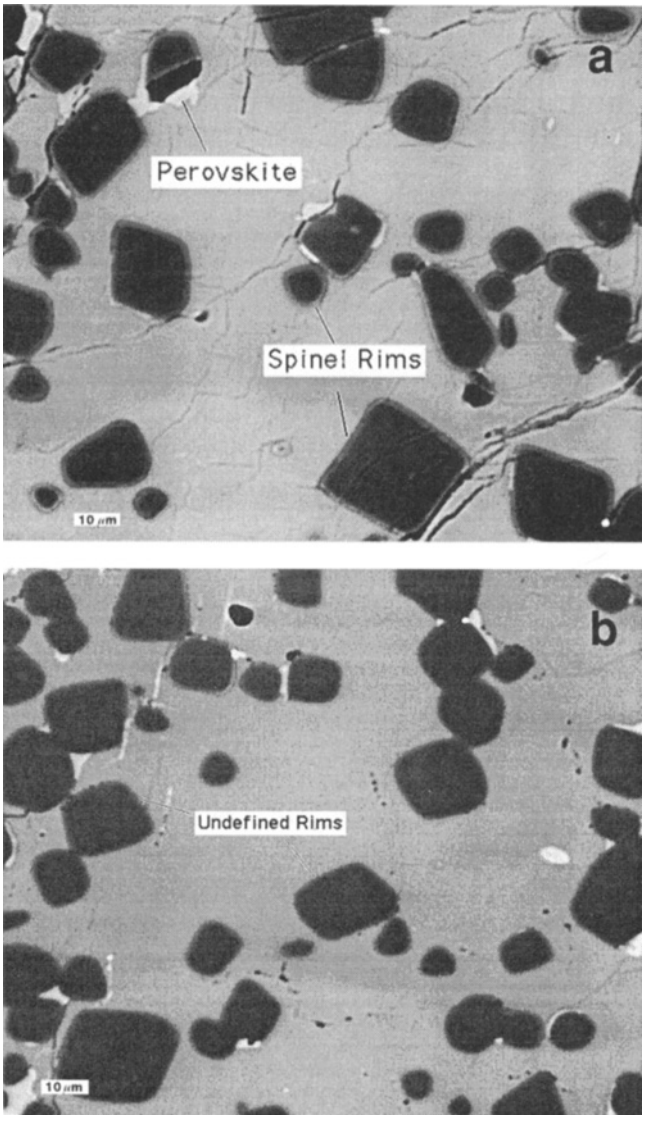

FIG. 4. (a) Backscatter electron image (×720, image size 135 × 170 μm) of spinels enclosed in anorthite from Leoville 3537-2. (b) Backscatter (×720, image size 135 × 170 μm) electron image of spinels in their host phase anorthite from Allende TS-23. Note that the rims or halos around grains within Leoville 3537-2 are more distinct than those from Allende TS-23. Rims around spinels are only present within grains enclosed by anorthite and rarely in grains close to the Wark–Lovering rim (enclosed by mantle melilite). The bright (white) phase is perovskite. And small bright thread-like features are alteration veins, typical of Allende CAIs. Such veins are absent in Leoville 3537-2.

defined as B1 CAIs from Allende. The core is dominated by melilite + fassaite + anorthite. Spinel occurs throughout the mantle melilite and core, for a total of 24 vol% in the studied section. The inclusion has experienced very little solid-state recrystallization or alteration, although some brittle deformation, typical of inclusions from Leoville, is observed. Spinels in the mantle melilite range from euhedral to anhedral, with most of the sub- to anhedral grains present around or within small inclusions of fassaite or within ~200 μm of the Wark–Lovering rims. Spinels located within core melilite and fassaite are typically euhedral.

Allende TS-23 has been previously described and studied (Beckett, 1986; MacPherson *et al.*, 1984; Simon *et al.*, 1991). It is a typical type B1 CAI from Allende, containing a mantle mainly composed of melilite and a core composed dominantly of melilite, fassaite, and anorthite. Spinels are present throughout the inclusion, representing ~18 vol% of the total thin section surface. This inclusion contains areas and veins of altered melilite typical of Allende inclusions (MacPherson *et al.*, 1984, 1988). The overall crystal habits of the spinels from Allende TS-23 are similar to those from Leoville 3537-2.

Backscatter imaging of spinels within anorthite grains from both inclusions show that most of these grains have thin rims or halo rounding them (Fig. 4). Perovskites are often associated with these rims, sometimes extending into the anorthite grains (brighter rims; Fig. 4a). In backscatter images, some rims are darker than the anorthite but brighter than spinel. These rims are much more abundant or at least more distinct around spinels in Leoville 3537-2 (Fig. 4a) than in Allende TS-23 (Fig. 4b), with essentially all spinels in anorthite having rims. X-ray maps suggest that high Mg and minor Ca dominate these rims; however, they are too thin for quantitative analysis. Because anorthite is the last phase to crystallize, these rims may represent either the last drops of liquid or a reaction between the spinels and last liquid that is predicted to occur at some point in the crystallization history of these objects (Stolper, 1982; Stolper and Paque, 1986).

Analyses of regions of silicate host phases immediately adjacent to the spinels were examined and are listed in Tables 3 and 4.

Minor Element Concentrations in Spinels

The areas studied (Figs. 1 and 2) were chosen for their location within the inclusions; however, we will show that the petrographic context (*e.g.*, the host silicate phases) is also important. We discuss our results in the form of interelement correlation plots for each meteorite separately, but with the same scales to simplify intermeteorite comparisons. All minor elements are represented by <5000 ppmw with the exception of Fe. No correlation exists between the size of the spinel grains analyzed and their minor element concentrations. Because of the high electron currents and long counting times, counting statistics errors are not significant for any of the plots and are not much larger than the size of the symbols (see Tables 1 and 2). Minor element data are for Leoville 3537-2 and Allende TS-23 are listed in Tables 1 and 2. We focus here on Ti, Cr, Fe, and V abundances. Calcium concentrations are possibly subject to correction for continuum secondary fluorescence so are not discussed. Analyses with Si values above 1000 ppmw were eliminated from our data set because we cannot prove that such analyses do not represent contamination that is derived from an overlap of the beam with host silicates. We do not discuss the significance of Si concentrations below 1000 ppmw because, at least in part, such value may represent contamination from section polishing.

Iron *versus* Vanadium

Figure 5a shows that V and Fe are not correlated for Leoville 3537-2. Although there is some overlap, the distributions in V concentrations from the edge, middle, and center regions are relatively well resolved. Spinels from the edge region contain systematically higher V, yet a smaller range (2700–3700 ppmw) than the middle (1600–3200 ppmw) or center (1500–2800 ppmw). The majority of grains have low-Fe contents of approximately 220–770 ppmw, with a sharp cutoff at 220 ppmw. The observed lower limit is not an analytical artifact (see Table 1) and may represent a measure of the primary Fe content of this CAI (as opposed to Fe added by secondary alteration processes).

TABLE 3. Electron microprobe analyses of host silicate phases for spinels investigated within Leoville 3537-2.

Sample #	Host	Na_2O	MgO	Al_2O_3	SiO_2	CaO	TiO_2	FeO	V_2O_3	Totals
Edge 1										
sp1,2	Mel	bd	3.22	28.89	27.30	41.77	0.06	bd	bd	101.31
sp5,6	Mel	bd	3.42	28.32	26.97	41.28	bd	bd	bd	100.10
sp8	Mel	bd	3.60	27.82	27.95	41.87	0.04	bd	bd	101.30
sp11	Mel	bd	4.19	26.26	28.43	42.03	0.04	bd	bd	101.02
sp15,14	Mel	bd	4.26	26.44	28.63	42.23	0.06	bd	bd	101.64
sp17	Mel	0.08	5.70	22.15	30.75	41.45	0.05	0.04	bd	100.28
sp18	Mel	bd	4.38	26.18	28.92	41.23	bd	0.05	bd	100.82
sp19	Mel	bd	3.19	29.25	27.11	41.59	bd	bd	bd	101.17
Edge 2										
sp1,2	Mel	bd	3.49	27.55	26.86	41.43	bd	bd	bd	99.37
sp7	Mel	bd	2.91	29.60	26.04	41.61	bd	0.10	bd	100.29
sp8-1	Mel	bd	2.11	31.91	25.36	39.50	bd	0.21	bd	99.15
sp12	Mel	bd	3.14	29.26	26.77	41.01	0.06	0.06	bd	100.33
sp14	Mel	bd	3.83	26.75	27.85	41.92	0.04	bd	0.04	100.46
sp18-2	Fs	bd	8.72	18.94	38.06	24.92	8.08	bd	0.42	99.21
sp17	Fs	bd	7.89	21.33	36.63	25.29	8.84	bd	0.43	100.48
sp18	Fs	bd	8.07	21.29	37.09	25.46	8.26	bd	0.42	100.64
sp20	Fs	bd	8.70	19.37	38.32	24.97	8.80	bd	0.47	100.65
sp21	Fs	bd	9.07	18.45	36.90	25.27	8.76	0.05	0.46	98.99
Mid 1										
sp1	Fs	bd	8.96	18.18	37.91	24.98	8.96	bd	0.47	99.51
sp4	Fs	bd	9.42	18.22	39.15	25.40	6.96	0.10	0.31	99.58
sp5	Fs	bd	9.42	17.83	38.49	25.06	7.32	bd	0.31	98.48
sp9,10	Fs	bd	7.89	21.42	36.69	25.44	8.66	bd	0.41	100.52
sp13	Fs	bd	9.61	18.89	39.88	25.40	6.93	0.08	0.31	101.13
sp14,15	Fs	bd	9.50	18.05	39.63	25.67	6.94	bd	0.26	100.06
sp16	Fs	bd	10.23	17.92	41.17	25.72	6.05	bd	0.27	101.41
sp17	Mel	0.14	7.70	17.52	33.80	41.72	bd	bd	bd	100.94
sp18	Mel	0.06	6.13	20.61	31.45	40.62	0.04	bd	bd	98.97
Mid 2										
sp2,3	Fs	bd	9.61	18.19	39.40	25.73	6.37	bd	0.23	99.59
sp4,5	Fs	bd	9.34	18.32	38.67	25.90	7.13	bd	0.37	99.77
sp7	Fs	bd	10.80	18.16	41.55	25.88	4.70	bd	0.19	101.31
sp8	Mel	0.13	7.69	17.80	33.22	41.79	0.04	0.10	bd	100.78
sp9,10	Mel	0.05	7.66	17.88	33.77	40.83	bd	bd	bd	100.22
sp14,15	Mel	0.09	8.07	17.22	34.54	41.13	bd	bd	bd	101.08
sp17,18	Mel	0.08	7.42	18.39	33.01	41.46	bd	bd	bd	100.42
sp20	Fs	bd	9.03	21.37	39.26	25.67	5.44	bd	0.18	100.98
sp23	An	0.10	1.18	35.26	42.58	19.27	bd	0.04	bd	98.48
sp25	An	0.10	0.08	36.89	43.31	20.71	0.05	bd	bd	101.16
sp26,27	An	0.10	0.36	35.69	42.10	20.73	0.05	0.24	bd	99.31
sp28	An	0.07	0.12	36.58	42.93	20.68	0.04	bd	bd	100.44
sp32	An	0.05	0.07	36.55	42.60	20.67	0.10	0.05	bd	100.11
sp34	Mel	0.21	8.73	14.81	36.38	40.85	bd	0.13	bd	101.16
Cen 1										
sp1	An	0.11	0.65	35.68	42.51	20.34	bd	0.07	bd	99.41
sp2	Mel	0.14	9.95	12.46	37.75	40.42	0.22	bd	bd	100.98
sp3	Fs	bd	11.90	16.29	44.35	25.87	2.62	bd	0.04	101.11
sp5	Fs	bd	11.00	17.04	41.32	25.71	4.34	bd	0.07	99.51
sp7	Mel	0.14	8.20	16.48	34.86	42.15	bd	bd	bd	101.87
sp8,9	An	0.05	0.12	36.73	42.95	20.58	0.08	bd	bd	100.54
sp10	An	0.04	0.13	36.80	43.26	20.63	0.07	bd	bd	101.00
sp12	An	0.13	0.13	36.72	43.48	20.53	0.04	bd	bd	101.07
sp13,14	An	0.08	0.47	37.69	43.19	20.33	0.04	bd	bd	101.81
sp15	Fs	bd	11.21	16.40	42.72	25.81	4.36	bd	0.08	100.66
sp16	Mel	0.08	8.59	15.26	35.05	41.71	bd	bd	bd	100.73
Cen 2										
sp4,5,6	An	0.09	0.21	36.54	42.85	20.41	bd	bd	bd	100.18
sp 7	An	0.07	0.23	36.75	43.47	20.43	0.08	bd	bd	101.08
sp 8	An	0.08	0.20	36.29	42.87	20.39	bd	0.09	bd	99.96
sp 9	An	0.07	0.13	36.43	42.83	20.60	0.04	bd	bd	100.14
sp12	Fs	bd	11.17	17.10	42.60	25.92	4.06	bd	0.08	100.95
sp 13	An	0.08	0.33	37.12	43.64	20.66	bd	bd	bd	101.90

TABLE 3. *Continued.*

Sample #	Host	Na_2O	MgO	Al_2O_3	SiO_2	CaO	TiO_2	FeO	V_2O_3	Totals
Cen 2 *(continued)*										
sp14	Mel	0.21	9.70	12.04	37.12	41.80	bd	bd	bd	100.92
sp15	Mel	0.20	10.05	10.84	38.70	40.00	0.07	bd	bd	99.96
sp16	Fs	bd	11.03	16.82	41.99	25.97	4.37	bd	0.09	100.30
sp18	Fs	bd	9.56	20.37	39.78	25.62	4.70	bd	0.20	100.28
sp19	Fs	bd	8.90	21.65	39.16	25.88	5.63	bd	0.29	101.52
sp20	Fs	bd	8.52	20.95	37.36	25.97	6.95	bd	0.30	100.10
sp23	Fs	bd	9.38	19.31	36.53	27.24	4.48	bd	0.17	97.16
sp25	Mel	bd	6.91	19.76	32.66	41.59	0.07	bd	bd	101.03
sp26	Fs	bd	11.32	16.82	42.77	25.93	3.90	0.05	0.06	100.88
sp28	Fs	bd	8.63	21.51	38.29	25.52	6.32	bd	0.25	100.54
sp 29	Fs	bd	9.08	21.43	39.51	25.83	5.19	0.04	0.24	101.34
sp 30	Fs	bd	8.84	21.31	38.59	25.74	6.21	bd	0.26	101.00
sp33	Mel	0.18	10.27	10.97	38.26	41.75	bd	bd	bd	101.49
sp 34	An	0.12	0.47	36.26	43.01	19.97	bd	bd	bd	99.89

All analyses are reported as wt% oxide. Notes: Mel = melilite, Fs = fassaite, and An = anorthite.

TABLE 4. Electron microprobe analyses of host silicate phases of the spinels investigated within Allende TS-23. *

Sample #	Phase	Na_2O	MgO	Al_2O_3	SiO_2	CaO	TiO_2	FeO	V_2O_3	Oxide totals
Edge 1										
sp1	Mel	0.03	3.24	28.89	27.44	41.54	0.00	0.03	0.00	101.20
sp2	Mel	0.00	3.36	28.77	27.79	41.69	0.00	0.00	0.00	101.66
sp3	Mel	0.14	3.75	38.83	22.06	35.37	0.08	0.36	0.04	100.67
sp4	Mel	0.04	4.23	36.01	22.41	37.38	0.00	0.08	0.03	100.21
sp6	Mel	0.02	2.41	31.25	25.90	41.60	0.00	0.05	0.01	101.27
sp5	Mel	0.02	3.42	28.47	27.73	41.75	0.04	0.04	0.00	101.50
sp7	Mel	0.00	3.31	28.65	27.49	41.45	0.02	0.01	0.00	100.96
Edge 2										
sp1	Mel	0.01	3.55	27.70	27.99	41.34	0.03	0.00	0.00	100.64
sp3	Mel	0.02	4.24	26.42	29.30	41.90	0.00	0.04	0.03	102.04
sp7	Mel	0.02	3.68	27.94	28.18	41.46	0.02	0.04	0.00	101.40
Edge 3										
sp1	Mel	0.00	5.67	40.56	20.46	34.61	0.14	0.08	0.07	101.62
sp2	Mel	0.00	2.23	30.74	25.46	39.12	1.84	0.12	0.03	99.57
sp9	Mel	0.04	4.50	31.78	25.25	38.22	0.04	0.05	0.02	99.92
Mid 1										
sp 1	An	0.04	0.06	37.03	43.81	20.42	0.00	0.03	0.02	101.43
sp 2	An	0.08	0.12	36.54	43.42	20.00	0.06	0.00	0.04	100.30
sp 4	An	0.09	0.16	36.59	43.73	20.25	0.03	0.02	0.02	100.92
sp5	Mel	0.16	7.72	16.59	34.67	41.06	0.04	0.01	0.01	100.31
sp7,8,21	Mel	0.06	6.98	19.93	32.82	39.91	0.37	0.66	0.06	100.83
sp 9	Mel	0.16	7.37	18.05	34.46	41.42	0.00	0.03	0.00	101.53
sp 13	Mel	0.14	6.83	19.41	33.55	41.39	0.05	0.04	0.00	101.44
Mid 1										
sp 13	An	0.02	0.07	36.44	43.29	20.01	0.04	0.01	0.00	99.91
sp 14	Mel	0.18	7.85	16.84	35.33	41.48	0.02	0.04	0.03	101.80
Mid 1										
sp 15	Mel	0.09	7.01	19.38	33.55	41.15	0.00	0.04	0.00	101.24
sp 16,17	Mel	0.15	7.47	17.83	34.51	41.49	0.00	0.04	0.00	101.52
sp 18	Mel	0.03	2.84	22.53	39.11	34.58	0.05	0.65	0.02	99.82
sp 19	Mel	0.05	9.11	16.48	38.93	34.59	0.07	1.20	0.00	100.45
sp19	An	0.11	0.13	37.00	44.03	20.47	0.07	0.00	0.00	101.84
sp 20	Mel	0.10	7.67	18.77	35.11	37.78	1.37	0.44	0.07	101.34
Mid 3										
sp1	Mel	0.18	7.60	17.07	34.58	41.07	0.03	0.24	0.00	100.82
sp2	Mel	0.13	6.72	19.49	34.01	40.85	0.02	0.23	0.00	101.48
sp3	Mel	0.09	6.23	21.03	32.67	41.57	0.01	0.04	0.00	101.70
sp4	Mel	0.06	6.69	20.12	33.42	41.82	0.00	0.04	0.00	102.18
sp5	Mel	0.12	7.13	18.77	33.16	40.56	0.03	0.02	0.04	99.83
sp9	Fs	0.01	11.11	16.30	43.88	25.10	4.14	0.04	0.14	100.82
sp10	Fs	0.02	10.74	16.24	43.24	24.93	4.22	0.05	0.18	99.70

TABLE 4. *Continued.*

Sample #	Phase	Na_2O	MgO	Al_2O_3	SiO_2	CaO	TiO_2	FeO	V_2O_3	Oxide totals
Mid 3 *(continued)*										
sp11	An	0.10	0.12	36.87	44.00	20.03	0.02	0.04	0.02	101.21
sp12	An	0.11	0.12	36.97	44.24	20.17	0.03	0.02	0.01	101.70
sp13,14	An	0.00	12.68	13.20	47.03	25.58	3.50	0.04	0.08	102.19
sp16	An	0.03	0.06	36.90	43.76	20.06	0.00	0.04	0.01	100.90
Cen 1										
sp1,2	Fs	0.02	10.38	18.04	42.78	25.28	4.40	0.02	0.11	101.12
sp1,2-2	Fs	0.00	11.20	17.05	44.02	25.42	4.10	0.02	0.12	101.98
sp3,4	Fs	0.00	9.68	20.02	41.43	25.36	4.84	0.00	0.07	101.49
sp5	Fs	0.00	10.10	18.02	42.02	25.05	5.09	0.00	0.16	100.52
Cen 1										
sp6	Fs	0.01	9.51	19.59	40.80	25.04	5.40	0.00	0.09	100.57
sp7	Mel	0.00	11.32	12.35	40.35	35.88	0.32	0.18	0.08	100.52
sp8	Mel	0.09	8.22	11.37	43.34	33.17	0.04	0.16	0.00	96.44
Cen 1										
sp9	Mel	0.18	8.59	14.60	36.34	40.99	0.00	0.01	0.01	100.76
sp10	Mel	0.05	6.09	18.05	39.01	36.98	0.06	0.14	0.00	100.39
Cen 2										
sp17	Mel	0.15	7.37	17.70	34.39	40.83	0.05	0.01	0.00	100.51
sp15	Mel	0.16	7.53	18.44	33.69	40.05	0.04	0.00	0.00	99.93
sp14	Mel	0.15	7.95	16.37	35.20	41.19	0.02	0.02	0.00	100.93
sp1,2,3	Fs	0.01	12.92	12.70	47.12	25.43	3.39	0.01	0.08	101.72
sp4-1	Fs	0.00	9.71	18.06	40.75	24.86	6.18	0.06	0.35	100.03
sp4-2	Fs	0.00	9.65	19.68	40.79	25.54	5.74	0.03	0.14	101.61
sp6	Fs	0.02	9.29	19.35	39.54	24.85	7.44	0.03	0.18	100.77
sp8	Fs	0.17	8.02	16.37	35.58	41.17	0.02	0.02	0.02	101.43
sp10	Fs	0.00	9.64	20.36	40.61	25.40	5.35	0.00	0.12	101.56
sp11	Fs	0.00	11.20	17.34	44.51	25.70	3.15	0.01	0.10	102.05
sp12	Mel	0.10	7.16	18.35	33.90	41.23	0.01	0.04	0.02	100.83
sp13,14	Mel	0.15	7.31	17.73	34.00	40.78	0.02	0.00	0.00	100.03
sp15	Mel	0.17	7.76	16.09	34.65	40.47	0.06	0.01	0.02	99.32

*All analyses are in wt% oxide. Notes: Mel = melilite, Fs = fassaite, and An = anorthite.

Spinel grains from Allende TS-23 (Fig. 5b) also show no correlation between V and Fe concentrations. The range in V concentration (930-2770 ppmw) is lower than that of Leoville 3537-2, but Allende TS-23 has a much wider range in Fe contents (290–44 000 ppmw). As with Leoville 3537-2, edge grains have the highest V concentrations ranging from 180–2770 ppmw and contain the largest concentrations of Fe (up to 4.4%), but low-Fe grains are also present in each of the three edge regions (as low as 300 ppmw). Spinels from the center and middle areas overlap significantly, but the lowest V grains are in the center regions

Vanadium *versus* Titanium

Spinels from Leoville 3537-2 show a reasonable correlation between V and Ti for the center and middle areas, whereas most grains from the edge area plot as a separate group (Fig. 6a). All grains with Ti > 3000 ppmw are inclusions in fassaite. If edge grains are restricted to those in (or between) mantle melilites, a discrete edge population results with V greater than about 2700 ppmw and Ti < 2300 ppmw. The center and middle areas have a much wider range in Ti (approximately 600–4200 ppmw) than the majority of edge area grains. The grains with both the lowest V and Ti are from the center.

In Allende TS-23 (Fig. 6b), both Ti and V concentrations show a smaller range than in Leoville 3537-2. Taken independently, the center and most of the middle area spinels show a significant correlation, which is suppressed due to our requirement of having the same scale for a and b in Fig. 6. As with Leoville 3537-2, Allende TS-23 edge spinels have the highest V concentrations.

Plotting grains according to their host minerals in Leoville 3537-2 (Fig. 7) shows that with some overlap, four different populations and at least two (possibly three) trends are distinguished. Grains from the middle and center areas that are enclosed by melilite (Fig. 7a) define a positive slope distinct from grains within the edge area. The edge population may define another trend with a negative slope. Grains enclosed by fassaite (Fig. 7b) show a positive V-Ti correlation and define a compositional field essentially distinct from that of spinels in melilite. Spinels enclosed by anorthite (Fig. 7c) plot as a field intermediate between those of melilite and fassaite with the most restricted range in Ti (approximately 1000–2600 ppmw) and V (approximately 1900–2700 ppmw). However, the lowest concentration grains in all host phases are similar.

As observed in Leoville 3537-2, the spinels from Allende TS-23 that are enclosed by melilite show a different trend than those enclosed by fassaite and anorthite (Fig. 8a,b). The trends observed in Allende TS-23 are similar to those of Leoville 3537-2; however, those spinels enclosed in fassaite have different Ti and V concentrations than those of Leoville 3537-2, and the positive V-Ti correlation for spinels in fassaite is not as well defined for Allende TS-23.

Chromium *versus* Titanium

In Leoville 3537-2, Cr shows a slight but significant negative correlation with Ti (Fig. 9a) with the trend defined by the center and middle areas. The overall range in Cr is a factor of ~2 (a factor of 1.4 if only middle and center grains are considered). Omitting the edge

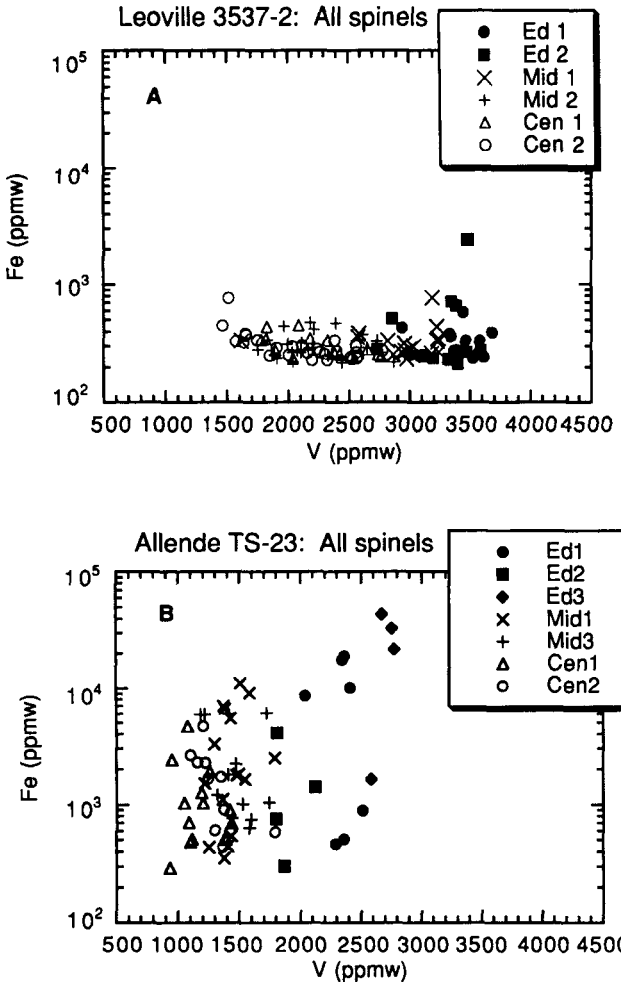

FIG. 5. Log-linear plots (Fe to V ppmw), both at the same scales, for Leoville (a) and Allende TS-23 (b) spinels. Counting statistics errors (Tables 1 and 2) are only slightly larger than the size of the symbols. Edge spinels are plotted as closed symbols; middle and center are plotted as open symbols. (a) The overall Fe pattern for these Leoville 3537-2 grains is relatively flat with increasing V. Most of the edge grains have the highest V concentrations. The flat pattern at ~300 ppmw Fe concentrations is not an analytical artifact. (b) Large scatter exists within the Fe concentration of these Allende TS-23 spinel grains. The highest Fe values are found in edge spinels but, compared with (a), considerable scatter also exists in middle and center grains. As with Leoville 3537-2, edge grains have the highest V values.

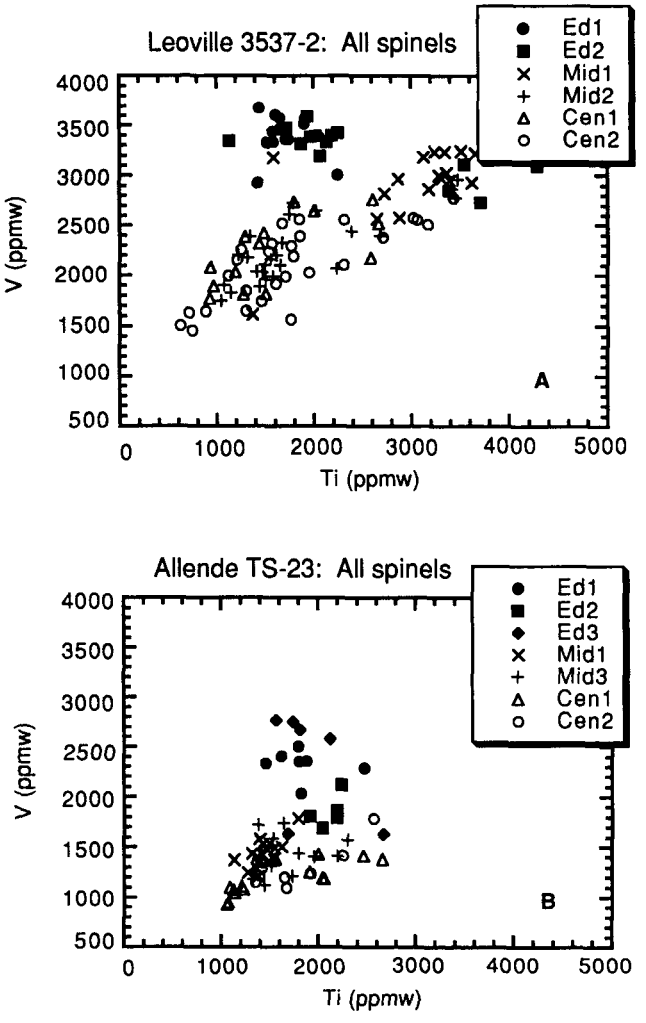

FIG. 6. Two graphs of V to Ti (ppmw), both at the same scale, of Leoville 3537-2 (a) and Allende TS-23 (b) spinels. Counting statistics errors (Tables 1 and 2) are approximately equal to the size of the symbol. Edge spinels are plotted as closed symbols; middle and center are plotted as open symbols. Both plots show that V to Ti is positively correlated, although the overall pattern is better defined in (a). Most edge grains plot as a separate population to the left and above the middle and center grains. Leoville 3537-2, however, does have a few edge grains enclosed within pyroxene that have high-Ti values similar to most mid grains.

grains included in fassaite (high-Ti concentrations), the mantle melilite edge grains (edge grains <2100 ppmw Ti) define a distinct field.

Unlike Ti, the compositional range for Cr in Allende TS-23 spinels (Fig. 9b) is greater than in Leoville 3537-2, and a stronger negative correlation is observed among center and middle grains with many grains showing 1500–2000 ppmw Cr. Unlike Leoville 3537-2, there is a potential for two groups of edge spinels in Allende TS-23: one possibly similar to Leoville 3537-2 with a range in Cr concentration from approximately 500–1000 ppmw (much lower in Cr than the middle-center trend) and one plotting close to the Ti axis, with Cr < 1000 ppmw. Additional sampling, however, might show these two groups to be endmembers of one large, nearly vertical trend.

Chromium *versus* Vanadium

Chromium also shows a somewhat tight trend having a negative correlation with V in Leoville 3537-2 spinels (Fig. 10a). Edge grains have the highest V values and the lowest Cr (down to ~80 ppmw). Center grains have the highest Cr values, up to 1400 ppmw.

Spinels from Allende TS-23 show larger scatter than for Leoville 3537-2 (Fig. 10b). Like Leoville, edge grains tend to have the highest V concentrations but the lowest Cr. Similarly, the center grains are the richest in Cr, up to ~2000 ppmw. Overall TS-23 has a larger range in Cr (approximately 500–2000 ppmw) compared with 3537-2 (approximately 800–1400 ppmw, with one exception of ~1700 ppmw).

Iron *versus* Chromium

For Leoville 3537-2, the Fe–Cr field is quite restricted (Fig. 11a). For Allende TS-23, however, even excluding the striking population of low-Cr edge grains, the Fe and Cr concentrations are significantly more variable (Fig. 11b). Within the edge spinels from Allende TS-23, there is a suggestion of an anticorrelation: those grains with the highest Fe (4.4%) have the lowest Cr (450 ppmw). However, not all the edge area spinels in melilite have low Cr values.

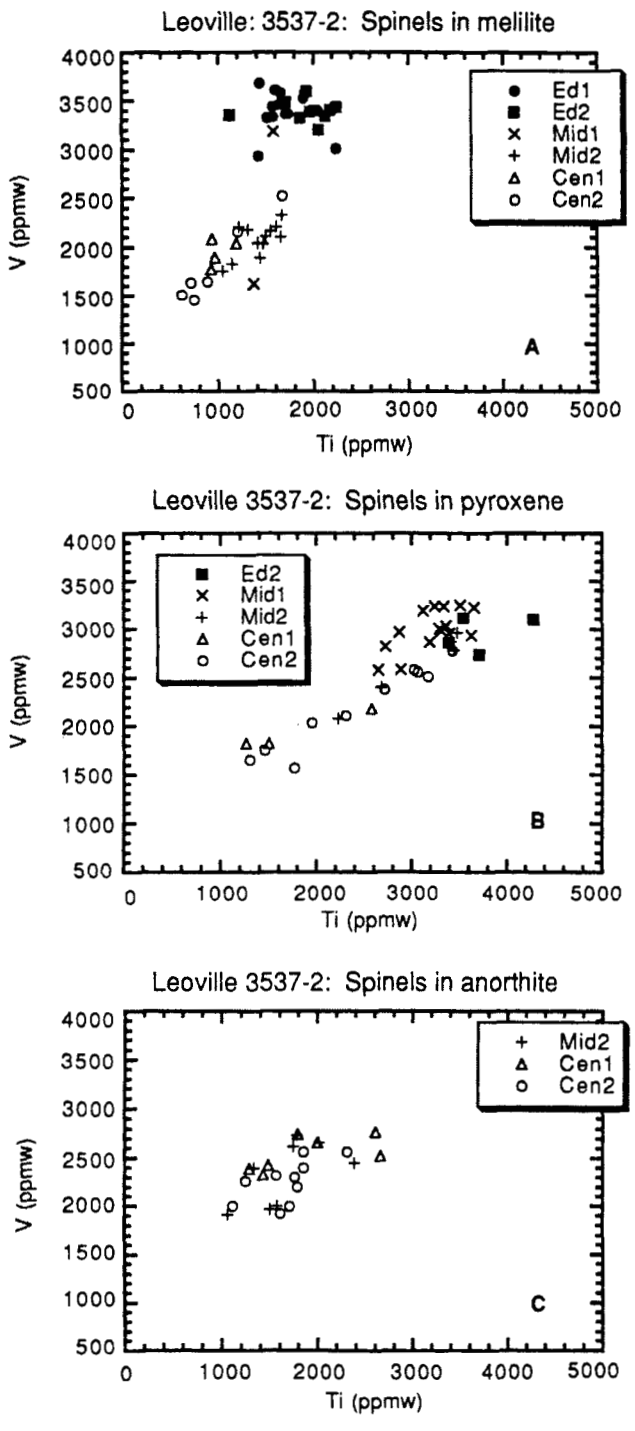

FIG. 7. Three graphs of spinel grains from Leoville 3537-2 separated according to their host silicate phase. All graphs have the same scales. Edge spinels are plotted as closed symbol, whereas middle and center are plotted as open symbols. Counting statistics errors (Table 1) are approximately equal to the size of the symbol. Shown in (a) is a plot of spinel grains enclosed within melilite, (b) is a plot of grains enclosed within fassaite, and (c) is a plot of grains enclosed within anorthite. Grains within melilite and fassaite define two different trends, sharing common low-Ti and V end points. Those enclosed in fassaite have the highest Ti, whereas those enclosed in melilite have the highest V values. Edge grains in fassaite define a separate population. Grains within anorthite have V and Ti values intermediate to melilite and fassaite, but the lowest concentration grains are similar in all host phases.

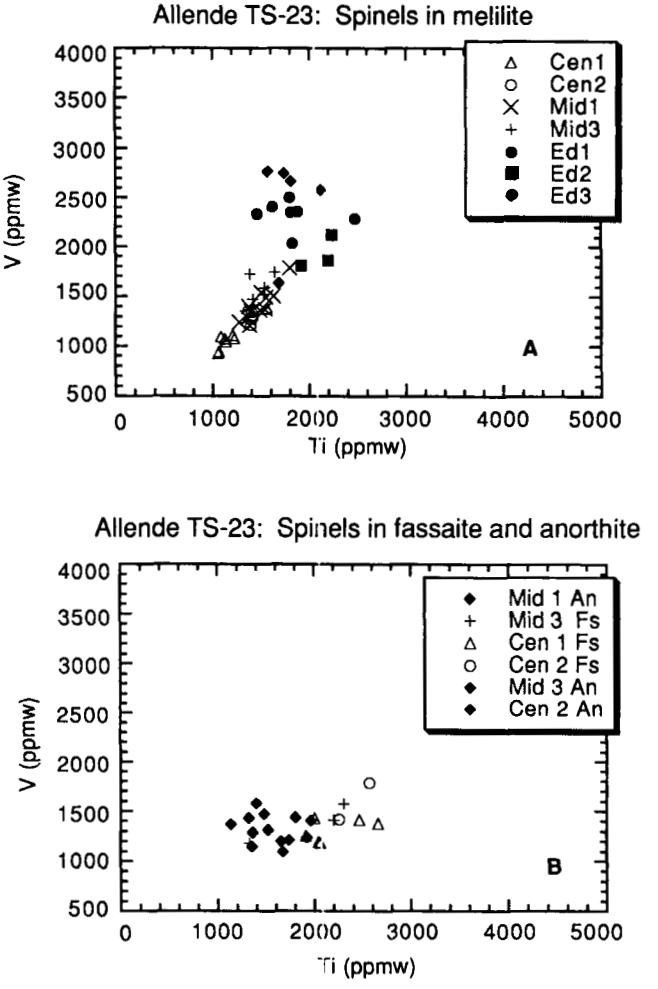

FIG. 8. Vanadium–titanium correlations for spinels from Allende TS-23, enclosed within melilite (a) and enclosed within fassaite and anorthite (b). Both graphs have the same scales. Edge spinels are plotted as closed symbols; middle and center are plotted as open symbols. Counting statistics errors (Table 2) are approximately equal to the size of the symbol. As with Leoville 3537-2 (Fig. 7), three different trends are formed from grains enclosed in melilite, and fassaite plus anorthite. Except for a better-defined fassaite trend in Leoville, both inclusions show the same groupings/trends.

Relationship between Minor Elements and Host Silicate Phase

We have investigated the local composition of the host silicate phases for each spinel analyzed. For the Leoville inclusion, there is some correlation between the Ti content of the spinels and the Ti concentration of the fassaites (Fig. 12a), but none is observed for Allende (Fig. 12b). A similar positive trend for a different Allende inclusion was reported by Meeker *et al.* (1983). Furthermore, there is a negative correlation between the Åk content of adjacent melilites and the Ti concentrations of their enclosed spinels. No other elemental (for those we explored) correlations exist between host silicates and spinels.

DISCUSSION

Spinel Crystal Chemistry

The spinels we investigated are all $MgAl_2O_4$, *sensu stricto*, having a normal cubic crystal structure. There is a continuous replacement series from spinel to hercynite ($Fe^{+2}Al_2O_4$) showing that divalent Fe substitutes easily for Mg. The general formula for spinel can be written as AB_2X_4, where A is the tetrahedral site and

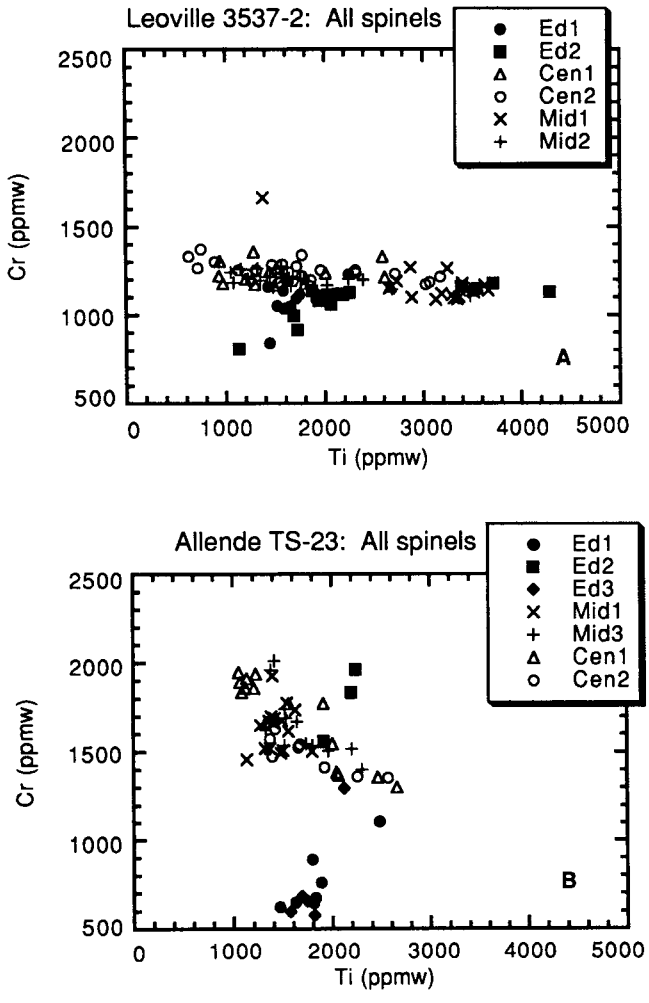

FIG. 9. Chromium *vs.* Ti correlations, both at the same scale, for Leoville 3537-2 (a) and Allende TS-23 (b) spinels. Counting statistics errors (Tables 1 and 2) are approximately equal to the size of the symbols. Edge spinels are plotted as closed symbols; middle and center are plotted as open symbols. Many edge grains from Allende TS-23—compare (b)—plot as a distinct group with low-Cr values.

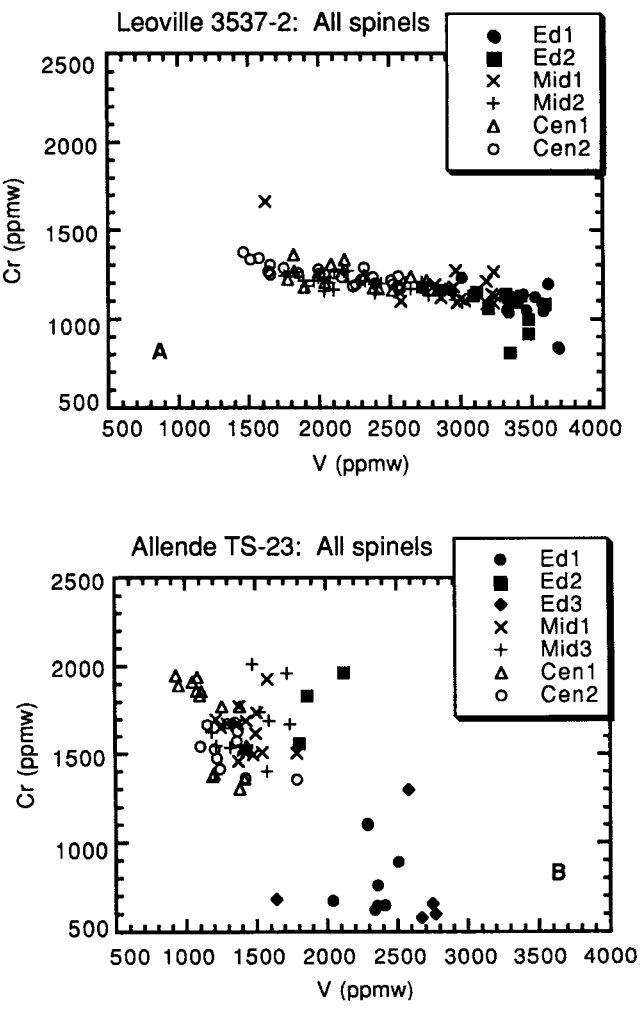

FIG. 10. Chromium *vs.* V correlations for Leoville 3537-2 (a) and Allende TS-23 (b) spinels (both plotted at the same scale). Counting statistics errors (Table 1 and 2) are approximately equal to the size of the symbols. A clear negative correlation exists for grains from Leoville, with a well-defined trend: the higher the V, the lower the Cr concentrations. Allende TS-23, however, does not show a well-defined trend.

B is the octahedral site. By considering both charge and ionic radius, we expect V^{+2}, Cr^{+2}, and Fe^{+2} to substitute for Mg; whereas we expect Cr^{+3}, V^{+3}, Fe^{3+}, Ti^{+3}, and Ti^{+4} to substitute for Al. Although the precision of our data is very good, with the exception of spinel with the highest Fe values, the concentrations of all minor elements are still too low to distinguish true variations in their cation proportions from the analytical error in the major element data. For example, the maximum variation in Cr for Allende TS-23 (Fig. 11b), if trivalent, would produce only a 0.3% decrease in the measured Al, which is approximately equal to the Al counting statistics standard deviation. In some spinels from Allende TS-23 (spinels with >1 wt% Fe), our data suggest that Fe is present within these Fe-rich grains as both ferric and ferrous, but complications due to variations in other minor elements prohibit quantitative proportions from being obtained.

Recording Alteration: Interpreting the Role of Iron, Chromium, and Vanadium

Our major interpretational challenge is to explain the distinct groupings as a function of location and host phase shown in Figs. 6 and 7. We begin by considering the role of postcrystallization alteration. Inclusion TS-23 is typical of Allende type B CAIs in showing veins of secondary alteration phases (*e.g.*, MacPherson *et al.*, 1988). Leoville 3537-2, however, is essentially unaltered, experiencing "only slight solid state recrystallization of melilite" (Caillet *et al.*, 1993) and some secondary calcite.

It is generally accepted that enrichments of Fe within spinels from Allende type B CAIs occurred postcrystallization. In TS-23, we observe no correlation between Fe-rich spinels and their proximity to alteration veins. Grains with the highest Fe concentrations are found near the margins (Wark–Lovering rim) of the objects. Such grains were affected by a postcrystallization event that may not have been concurrent with vein alteration. The close proximity of these Fe-rich grains to the CAIs exterior suggest that this geographic location within the objects contributed to easier alteration of this area compared with the core, either by gas–solid exchange in the nebula or processes within a parent body.

Our data show (Fig. 5) a difference of approximately two orders of magnitude in Fe concentrations between the most Fe-rich grains in Allende TS-23 and essentially all spinels in Leoville 3537-2. The Fe enrichments >1000 ppmw exhibited by grains within the middle

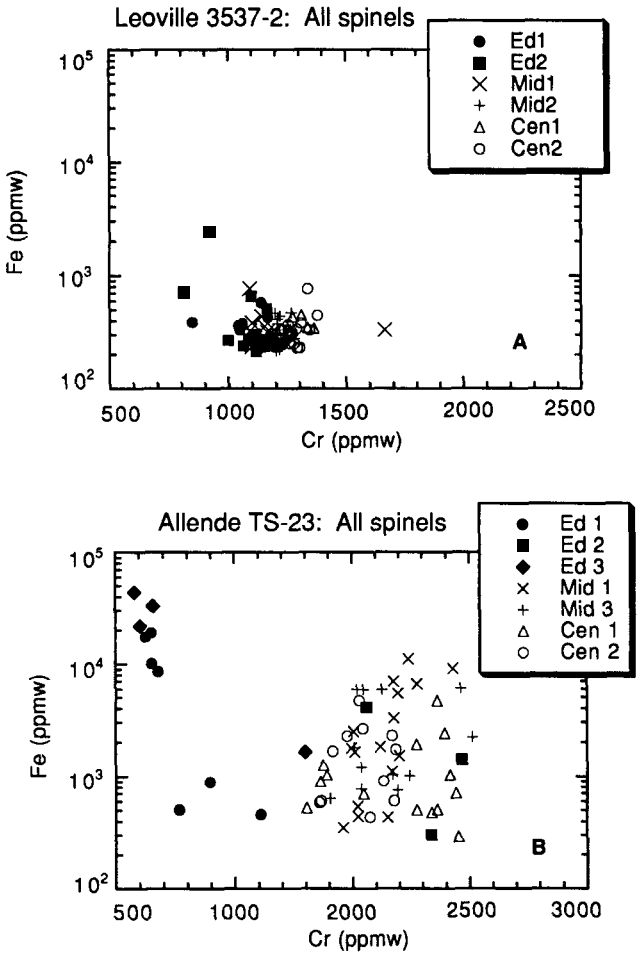

FIG. 11. Iron *vs.* Cr, both at the same scale, of Leoville 3537-2 (a) and Allende TS-23 (b) spinels. Counting statistics errors (Tables 1 and 2) are approximately equal to the size of the symbol. Edge spinels are plotted as closed symbols; middle and center are plotted as open symbols. Most grains from Leoville 3537-2 (a) plot as a group, whereas those from Allende TS-23 (b) show a large scatter in both Fe and Cr. The presence of such high-Fe values is attributed to alteration postcrystallization. The cause of the low-Cr, high-Fe grains is less certain.

and center areas in Allende TS-23 may also be due to an alteration event, despite the lack of correlation between their proximity to veins of alteration and Fe abundances. It is also possible, however, that the primary Fe concentrations vary by an order of magnitude among type B CAIs. This is an alternative interpretation of the larger Fe contents in Allende TS-23 spinels.

The relatively narrow range of observed Fe concentrations for the majority of Leoville 3537-2 spinels is most easily explained by igneous crystallization, which is consistent with the overall unaltered appearance of Leoville 3537-2. Similarly, spinel grains with low-Fe concentrations (<1000, probably <600 ppmw) within Allende TS-23 may also be unaltered; however, differences in the bulk composition between Allende TS-23 and Leoville 3537-2 may compromise this conclusion.

Because Cr is a relatively volatile element, it is prudent to consider its origin from some postcrystallization alteration event. As noted, the relatively tight distribution for Fe and Cr in Fig. 11a for Leoville 3537-2 is what we would expect if these grains were of igneous origin and unaffected by postcrystallization alteration. Excluding the edge area, the overall Cr concentration of spinels from Allende TS-23 is almost a factor of 2 higher than those from 3537-2 (Fig. 11). There is no correlation of Cr and Fe in Allende TS-23 spinels. Thus, if the excess Cr in spinels from Allende TS-23 is from postcrystallization alteration, the process is even more complex than previously recognized, possibly with the Cr and Fe introduced in different stages (epochs). Alternatively, we cannot rule out the possibility that the higher Cr in spinels from Allende TS-23 could reflect differences between the bulk compositions of the objects and be of igneous origin.

A striking feature of Fig. 11b is that many Fe-rich edge grains from Allende TS-23 have very low-Cr concentrations, which suggests that Cr may be preferentially removed as Fe is added. It is unclear to us how this would occur. If the higher Fe and Cr concentrations of the Allende TS-23 middle and edge spinels relative to Leoville 3537-2 are due to alteration (rather than bulk compositional differences), additional episodes of alteration might be indicated (*e.g.*, nebula for the interior and parent body only at the edge) with different behavior for Cr in each case. It may be simpler, however, to regard essentially all Cr as primary.

Although V is a refractory element, it is more volatile than Ti (*e.g.*, Wasson, 1985). Within some CAIs, V is highly concentrated in magnetites associated with Fremdlinge (MacPherson *et al.*, 1988). Because magnetites within Fremdlinge are interpreted as secondary products, it is reasonable to assume that some postcrystallization process also produced their V enrichments. The issue may be as simple as the V concentration within Fremdlinge magnetite may represent redistributed primary V from the host CAI. Therefore, we should consider the possibility that V enrichments within spinels were produced after crystallization. If V is of secondary (external) origin, correlations between it, Fe, and Cr (elements also suspected to be introduced during alteration events) are expected. Our data, however, show that V is not correlated with Fe enrichments except for a few grains near the margin of Allende TS-23, which have high Fe and V (Fig. 5b). Vanadium is also negatively correlated with Cr (Fig. 10), which is very difficult to explain if both elements were secondary. The overall higher V concentrations within spinels from Leoville 3537-2 likely reflect either real bulk compositional difference between the two inclusions or a sampling bias (*e.g.*, we just did not measure enough spinels in Allende TS-23). We conclude that there is little evidence for V of secondary origin.

Expectations from Single-Stage Fractional Crystallization

The large range in Ti concentrations in spinels from both inclusions (a factor of 6 in Leoville 3537-2 and a factor of 3 in Allende TS-23) is interesting (Figs. 6 and 7). We expect that if these CAIs crystallized at near-equilibrium conditions, almost no variation in Ti should exist. To interpret the significance of our result, it is first necessary to review some important facts concerning the crystallization history of type B CAIs.

The equilibrium crystallization sequence for an average type B CAI bulk composition is (in order of decreasing temperature) spinel–melilite–anorthite–fassaite (Stolper, 1982), spinel being the liquidus phase. For cooling rates faster than ~1 °C/h, the sequence changes to spinel–melilite–fassaite–anorthite (Stolper and Paque, 1986). The reversal of fassaite and anorthite is interpreted to be due to the difficulty in nucleating anorthite. The fine grain size of spinel constrains the maximum temperature experienced by type B CAIs to below the liquidus (Wark, 1987; Stolper, 1982). For 3 h heating times, the experiments of Stolper and Paque (1986) further constrain peak melting temperature to have been between 1400–1500 °C, the

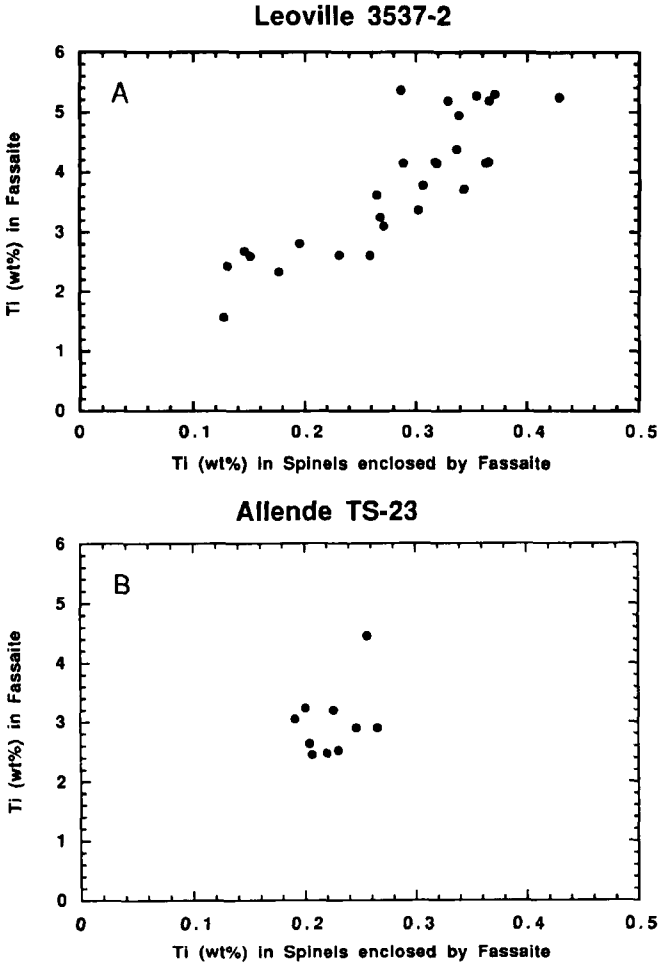

FIG. 12. A graph of the Ti concentration in adjacent fassaite against Ti within spinels enclosed by fassaite (wt%). (a) All spinels and host fassaite Ti values from Leoville 3537-2. A positive correlation exists. (b) All spinels and host fassaite Ti values from Allende TS-23. No correlation exists.

spinel + liquid field. Such peak temperatures produce euhedral melilite, higher temperatures producing dendritic textures not observed in natural materials. The experiments of Stolper (1982), Stolper and Paque (1986), and Paque (pers. comm.) indicate the maximum amount of spinel crystallization is around 11–12%.

Spinel crystallization ceases early, possibly when melilite appears, but by at most 50% total crystallization (compare also the crystallization models for Allende TS-23 given by Simon *et al.*, 1994). Spinels enclosed in anorthite are potentially important because these grains were likely in contact with liquid late in the crystallization history. Although not serrated, many of these spinel grains are more sub- to anhedral in form than those in fassaite or melilite, which suggests that they may have been reacting with the liquid either before and/or during anorthite crystallization (Fig. 4).

Scenario 1–For the middle and center grains (Figs. 7 and 8), there are several possible qualitative explanations for the positively correlated Ti–V trends and for the high Ti values. If we assume that both Ti and V are incompatible elements (V predominately as V^{+2}), then spinels with the lowest Ti and V concentrations are the first-formed. The total range of Ti and V concentration, however, should be very small (factor of 2 at most; comparable with Fe and Cr distributions for Leoville 3537-2, Fig. 10a). We cannot explain the entire range of observed Ti (and V) based on a single crystallization history using this scenario. The observed ranges for Ti and V are considerably larger than expected for single-stage crystallization. In the light of this, we have no explanation for the tightness of the Fe and Cr distributions in Leoville 3537-2.

Scenario 2 (Version 2a)–We assume that (1) Ti is incompatible, (2) V is slightly compatible, (primarily V^{+3}) with $D_{sp}(V) \cong 1$–1.5, and (3) spinel continues to crystallize throughout most of the cooling/crystallization cycle. Assumption (3) does ignore the experimental evidence discussed above for a limited range of spinel crystallization, but it is appropriate to constructively challenge the experimental results. In this scenario, initially formed spinels would have the lowest Ti and the highest V, possibly similar to the highest V edge grains in Fig. 6. As spinel crystallization proceeded, Ti became enriched and V slightly depleted in the melt, producing a trend with negative slope (Figs. 6–8). However, once melilite began to crystallize, the high modal abundance of melilite would causes the bulk D for V to be significantly less than 1. Melilite and spinel cocrystallization would produce a positive V–Ti trend, starting from the edge population. This is not observed, so it is unlikely that version 2a is the crystallization history of the objects.

Scenario 2 (Version 2b)–Relative to version 2a, we assume (1) that V is highly compatible in spinel, and most importantly, (2) that spinel and melilite cocrystallize from the onset of crystallization. Although assumption (2) is in conflict with all CAI experimental studies to date, a reasonable description of the V–Ti trends can be obtained. For simplicity, we consider only the Leoville 3537-2 data. As shown in Fig. 13, the first spinel to crystallize would have the composition indicated by point A. Continued spinel + melilite crystallization would produce the AB trend. Observed fassaite zoning patterns (Simon *et al.*, 1991) show that once fassaite appears, the bulk D for both V and Ti are >1. Thus, once fassaite began to crystallize at point B, the liquid would become depleted in Ti (assuming this to be highly compatible in fassaite), and somewhat less depleted in V (assuming moderate compatibility in fassaite). A trend would be produced with an apparent positive correlation, but with the last crystallizing spinel having the lowest V and Ti. The trend for the middle and center spinels (Fig. 6) could be interpreted this way. The lack of spinel inclusions in melilite with compositions toward the B end of the AB trend might be explained if a sampling

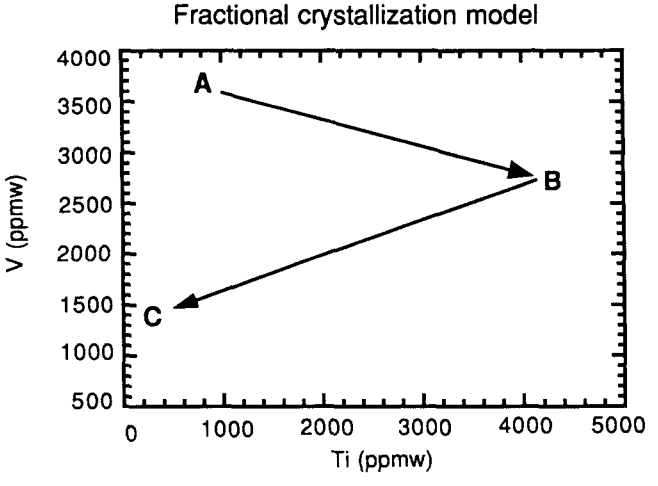

FIG. 13. Our single-stage igneous crystallization model for Leoville 3537-2, plotted as V *vs.* Ti. The scale is chosen to be identical to that of Fig. 6.

TABLE 5. Single-stage igneous crystallization model calculations.

	Required D (MA)	Observed D	Reference
D_{sp} (Ti)	0.14	0.19	Connolly and Burnett, 1999
D_{sp} (V)	5.6	1.4	Connolly and Burnett, 1999
D_f (Ti)	8.4	1.3–2.8	Simon *et al.*, 1991
D_f (V)	4.0	D(V) > D(Ti)	Simon *et al.*, 1991

bias exists (*i.e.*, we simply did not sample a location in the inclusion containing these grains). Table 5 shows the required partition coefficients for V and Ti to reproduce the Leoville 3537-2 data with this model. These cannot be ruled out with experimental data to date.

Several major problems exist with scenario 2b. For Leoville 3537-2, the highest Ti grains are inclusions within fassaites, and a large fraction of the lowest Ti grains are within melilites. Scenario 2b predicts that spinels located within fassaite should have the highest Ti values, and they do. Assuming that significant amounts of melilite continue to crystallize after fassaite appearance, however, there should be some spinels within melilite coexisting with fassaite in the middle or center regions that shows the high-Ti part of the BC trend, but none is observed. We should not find high-Ti spinels only in fassaite. We are willing to assume that a sampling problem may exist to explain why no spinel with high-Ti values exists within melilites (the high-Ti end of the AB trend), but this appears an unlikely explanation for melilite with spinels on the BC trend. The BC trend melilites with high-Ti spinel inclusions should coexist with fassaite. It is unreasonable that we would have missed them. It is possible that subsequent to fassaite appearance, additional crystallization of melilite is small. However, making this assumption leaves the low-Ti,V spinel inclusions in the middle and center melilites unexplained.

Depending on the efficiency at which fassaite and cocrystallizing melilites enclose spinels, scenario 2b also predicts that spinels enclosed in anorthite should have a range of Ti and V values (anorthite is the last phase to crystallize), but this is not the observation. In addition, assuming that mantle melilite crystallized from the outer surface inwards (MacPherson *et al.*, 1988), we would expect to see some spinels that were the first to crystallize (high V with a range of Ti) within the center and middle areas as they would have been pushed towards the center, but we do not. Although not completely impossible, scenario 2b has considerable difficulties and formation of these objects appears more complex than a single-stage fractional crystallization model.

Edge Spinel Grains and Fractional Crystallization–Given the problems of scenario 2b, an alternative way to account for the edge grain compositions in a fractional crystallization model is to assume that the high-V edge spinels represent a relatively small amount of compatible trivalent V partitioning into spinel, with the V–Ti correlation for the middle and center areas being a consequence of the incompatibility of all Ti and divalent V. This would assume that there is no external O fugacity buffer in effect during crystallization, thus conserving the initial amounts of tri- and divalent V. There is no evidence for divalent V in silicate minerals or liquids, although it is well characterized in the laboratory (Greenwood and Earnshaw, 1985). Our discussion has also assumed that both tri- and tetravalent Ti is incompatible in spinel. Overall, this model alone still cannot account for the range in Ti concentrations; however, it could explain the edge grain populations, ignoring those of the middle and center regions.

Reequilibration of Spinels during Fractional Crystallization

The above discussion assumed that spinel minor element compositions would be governed by fractional crystallization. If reequilibration during crystallization were total, a relatively restricted compositional range would be expected, in contrast to the big variations observed. A more plausible scenario, however, is one in which spinels that are in contact with liquid equilibrate rapidly with changes in liquid composition during cooling, but their composition is frozen once they are incorporated as inclusions. This reequilibration model would produce a trend starting at A going to B during melilite crystallization and then from B to C subsequent to fassaite appearance (Fig. 13), analogous to scenario 2b above. But unlike scenario 2b, this model can explain why spinel inclusions in melilite show a range in Ti and V beyond expectations for single-stage fractional crystallization without ignoring experimental results on the limited range of spinel crystallization. An increasing V concentration in spinel inclusions in melilite with increasing Åk content would be expected, opposite to what is observed. In contrast, Figs. 7c and 12a can be explained with the lowest Ti spinels corresponding to the latest crystallizing phases. The lack of spinel inclusions in melilite corresponding to the high-Ti parts of both the AB and BC trends in Fig. 13, however, causes the same serious difficulty for this model as for scenario 2b. Furthermore, this model offers no explanation for the edge grains in Fig. 7a, and these would have to be regarded as relics.

Possible Effects of Disequilibrium Crystallization

An alternative interpretation is that the range of spinel Ti and V concentrations in melilite is due to disequilibrium crystallization in the sense of fractional crystallization occurring without interface equilibrium being maintained (*e.g.*, due to the formation of boundary layers). This could plausibly occur in the initial stages of crystallization. The most easily visualized model is to assume that (1) the precursor solids to the initial melting event contained no relic spinel and that this material was rapidly heated into the spinel + liquid field and (2) that V and Ti are both incompatible. Spinel growth would occur rapidly with excess V and Ti incorporated in proportions matching that of the liquid. These initial disequilibrium spinels could be preferentially incorporated in melilite. The fast-growing spinels would have high V and Ti but decreasing concentrations as growth slowed. The middle and center trends for melilite inclusions in Fig. 6 might be explained this way. Assuming all spinel crystallized prior to fassaite appearance, one would expect the same range of spinel compositions in melilite and fassaite, contrary to observation. Further, assuming that as refractory lithophile elements, the bulk V/Ti ratio is solar, then the spinels in melilite should define a mixing trend with a slope corresponding to the solar V/Ti. However, the observed trends define a slope with a much higher V/Ti ratio. Overall, there is no evidence for major disequilibrium incorporation of V and Ti.

Alternative Origins for Compositional Variations

Here we consider five additional possibilities beyond fractional crystallization, focusing on explaining the large range in Ti concentration: (a) Ti was initially not homogeneously distributed within the liquid, (b) Ti is increased significantly in later stages of crystallization due to contributions from slowly dissolving perovskites inherited from the precursors (Kennedy *et al.*, 1997), (c) there are extensive subsolidus increases in Ti, (d) many of the spinels are relic grains that predated the original melting and crystallization, or (e) many spinels formed in secondary partial melting events.

(a) Inhomogeneous Titanium Distribution in the Liquid–High-Ti regions of an inhomogeneous liquid might increase the appearance temperature of fassaite to the point where locally formed, Ti-rich spinels were preferentially incorporated in fassaite. If most spinel forms prior to fassaite, a correlation between local fassaite Ti and spinel Ti would not be expected, contrary to observation (Fig. 12). If the liquid inhomogeneity is the consequence of remelting, alternatives (a) and (e) are the same and are discussed below. If the initial liquid is postulated to retain inhomogeneities reflecting differences in dissolution rates of the solid precursor grains, a relatively rapid cooling rate is needed to maintain the liquid compositional inhomogeneities. Upper limits to cooling rates are set by (1) the lack of dendritic or skeletal melilite (Stolper and Paque, 1986), (2) the absence of residual glass for Leoville 3537-2 (because of alteration veins in Allende TS-23, residual glass cannot be ruled out for this inclusion), and (3) the apparent absence of melt inclusions. It is probably unlikely that Type B CAI cooling rates are slow enough to meet these constraints, and simultaneously, fast enough to maintain the required liquid heterogeneities. In the absence of direct experiments, however, this alternative cannot be completely ruled out.

(b) Contributions from Slow Perovskite Dissolution–Alternative (b) is a special case of (a), focusing on perovskite, a plausible precursor phase of CAIs. In order for slowly dissolving perovskites to contribute to the observed distribution of Ti in spinels, cocrystallization of fassaite and spinel must be assumed. This assumption ignores existing experimental evidence to the contrary. The dissolution of perovskites must also be timed just correctly for a spinel to sample the enriched Ti-liquid and then be trapped in fassaite rather than melilite, a phenomena that seems highly unlikely. Overall, we find this alternative implausible.

(c) Subsolidus Increases in Titanium–Subsolidus increases in Ti by postcrystallization heating could potentially explain the high-Ti concentrations in spinels within fassaite and cannot be completely ruled out. It is not obvious, however, that Ti would diffuse from the fassaite into the spinels where it is found in minor amounts and incompatible compared to the fassaite. It is more likely that Ti would diffuse from the spinels to the fassaite during a long period of subsolidus heating.

(d) Relic Spinels–We define relic spinels as either a condensate or a spinel that formed in a previous generation of CAIs (*i.e.*, a grain that existed prior to the original melting of these inclusions). In either case, the relics must be somehow incorporated into the precursor solids from which the observed CAIs formed. Potential relic melilite and fassaite grains have been identified (Paque, 1990; Meeker, 1995) in CAIs; however, the most likely candidates for relic grains are spinels. Spinel is the only major phase stable at the inferred maximum temperatures from which the observed CAIs formed (Stolper, 1982; Stolper and Paque, 1986).

Without any compositional constraints on what defines a relic spinel grain, it could be argued that all spinels with compositions that cannot be understood through a fractional crystallization model are relic. Somewhat surprisingly, even with this broad definition of a relic grain, it appears a relic origin for many of the studied spinels from Allende TS-23 and Leoville 3537-2 is improbable. Although the distribution of relic grains might not be completely random, it would be very unlikely to find a compositionally coherent population of relic grains preferentially concentrated in specific phases, especially a late crystallizing phase such as fassaite. The preceding argument does not necessarily apply to the edge grain populations, and therefore, these could be relic grains. It would be plausible to find relic grains trapped preferentially in the first melilite formed, which are likely within the inclusion's mantles. If edge spinels are relic grains, we would not expect to see a correlation between the Mg content (Åk content) of the melilites with either the Ti or V concentrations of adjacent spinel inclusions. In contrast, if the edge spinels cocrystallized with melilite, a correlation might be expected, and within the edge grains alone, none is observed. Another possible type of relic grain is direct nebular condensates that were preserved during melting and/or crystallization. Figure 14 compares the (Fe,Cr) compositional fields of our analyzed spinels to the calculated Fe and Cr concentration of $MgAl_2O_4$ spinel grains condensing from a gas of solar and 100× solar composition (Ebel and Grossman, pers. comm., 1998). None of our data are near the predicted condensate compositions. Therefore, based on these calculations only, it is unlikely that any of the analyzed spinels from Allende TS-23 or Leoville 3537-2 are nebula condensates that were either part of the inclusions' precursors or introduced into them while they were molten.

(e) Secondary Partial Remelting Event–The compositional correlation of spinel grains with host phases can be explained by a secondary partial remelting event that occurred after the primary melting and crystallization but before incorporation into the parent bodies. In this model, edge grains are best understood as relics (but see below). The lowest Ti and V concentrations, dominated by spinels from the center area, are explained by fractional crystallization, but this can account only for grains with a maximum of ~1500 ppm Ti. Spinel grains with the highest Ti concentrations from the middle areas are primarily inclusions within fassaite and are the most difficult to explain. However, if this secondary event melted pyroxene in greater proportions to spinel and melilite, a liquid locally rich in Ti would result. Assuming that spinels would crystallize from this secondary liquid, these spinels would be richer in Ti (and V). It is not necessary to have spinel and fassaite cocrystallize, but negligible melilite can form. Locally remelted

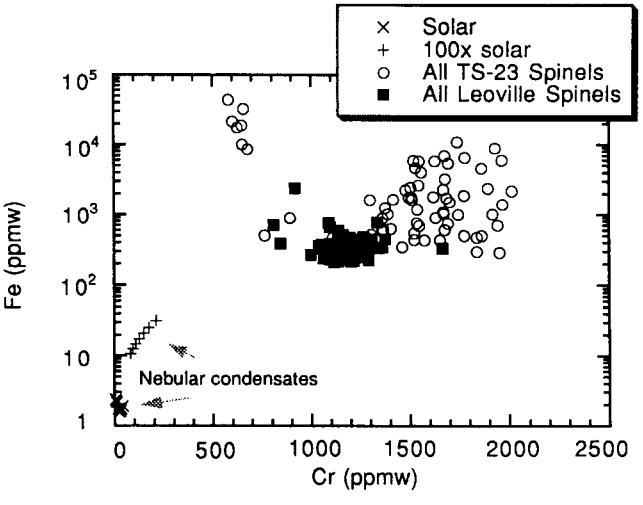

FIG. 14. A graph of Fe to Cr (ppmw), both at the same scale, of Leoville 3537-2 and Allende TS-23 spinels. Leoville 3537-2 spinels are plotted as closed symbols, and those from Allende TS-23 are plotted as open symbols. Plotted in the lower left corner are the Fe and Cr compositions of spinel grains predicted to condense from a gas of solar (×) and 100× solar (+) composition (Ebel and Grossman, pers. comm.). None of the analyzed spinels plot near the predicted condensate values, which suggests that they are not condensates.

regions that were rich in melilite would probably recrystallize the spinel and melilite, producing intermediate Ti concentrations for spinel inclusions in melilite between that of the first crystallized spinels and the Ti-rich grains produced by the secondary melting in fassaite-rich regions. It may be somewhat fortuitous that the middle region melilite inclusions appear to lie near the extension of the trend on Fig. 6b by the center grains. Remelting must be postulated for both inclusions, although proportionally fewer spinels in Allende TS-23 appear to have been affected. If it did occur, partial remelting appears not to be a special event in the history of just one object.

It is also possible that both the edge spinels and the remelting event postulated above to explain the Ti-rich spinels within fassaite might have been the result of the Wark–Lovering rim formation event. The popular model for Wark–Lovering rim formation has CAIs experiencing some type of rapid (flash) heating event that was intense enough to only melt at most the outer 100 μm (*e.g.*, Murrell and Burnett, 1987; Wark, 1997). Preferential evaporation of Si and Mg would enrich the residual surface melt in more refractory elements, although what scant data exist for Si and Mg isotopes suggests that little evaporation occurred. The low Cr in Allende TS-23 edge spinels might be due to this evaporation process. Amounts of Cr loss could vary with location, with fewer (but not all; see Figs. 9a and 10a) spinel grains from Leoville 3537-2 showing Cr loss. Upon cooling, perovskite and Wark–Lovering rim spinel crystallization would produce liquids relatively depleted in Ti but enriched in V. Spinels cocrystallizing with melilite from this evolved liquid could be rich in V and relatively high in Ti.

CONCLUSIONS

We have shown that by correlating minor element chemistry with their petrologic context, spinels in type B CAIs form interesting trends. Titanium and V are positively correlated, their overall concentrations defining four populations of grains: (1) those contained within the edge area (largely mantle melilite), (2) those contained with melilite, (3) those contained within fassaite, and (4) spinels within anorthite. It is unlikely that the overall range in Ti concentrations can be explained by a simple, one-stage melting model of CAI formation. The model with the fewest difficulties involves at least one additional melting event (possibly two) postdating the initial melting of the precursor grains. This model can explain the large range in Ti concentrations and the observed populations of spinels.

Our data also shows that Allende TS-23 spinels have experienced considerably more alteration than Leoville 3537-2, which is consistent with the overall petrology of the objects. Thus spinels are also markers for CAI alteration, recording the process(es) as increases in Fe concentrations and possibly decreases in Cr. The overall lack of Cr and Fe in Allende TS-23 suggests at least two episodes of alteration.

Although we can, in theory, account for spinels rich in Ti through additional melting events, it is difficult to explain the V-rich edge grain in the context of all other spinels. Therefore, it is possible that such grains could be relic in the sense of existing prior to the initial melting event. It is also possible that the V-rich edge grains are products from Wark–Lovering rim formation, although they are not obviously in the rim itself. The inability of this study to identify conclusively true relic grains might mean that either (a) type B CAI, unlike many chondrules, did not experience an epoch of fragmentation followed by reaccretion and subsequent melting, or (b) they may have been reprocessed (by multiple heating events?) so that any original precursor grains have simply been erased.

Acknowledgments–We would like to thank G. J. MacPherson for the loan of USNM Leoville 3537-2 and L. Grossman for the sample of Allende TS-23. This project was greatly improved by numerous conversations with J. Paque, J. Beckett, G. J. MacPherson, A. Davis, S. Russell, S. Simon, and L. Grossman, A. El Gorsey, R. Ash, and G. Rossman. We also thank D. Ebel and L. Grossman for data used in our condensation figure and P. Carpenter for assistance with the microprobe analysis. The quality of this manuscript was improved by constructive reviews from G. J. MacPherson, M. Ebihara, and associate editor J. S. Delaney, and we thank them. This project was supported by NASA grant NAG5-4319, D. S. Burnett.

Editorial handling: J. S. Delaney

REFERENCES

ARMSTRONG J. T. (1995) *CITZAF*: A package of correction programs for the quantitative electron microbeam x-ray analysis of thick polished material, thin films, and particles. *Microbeam Analysis* **4**, 177–200.

BECKETT J. R. (1986) The origin of calcium-aluminum-rich inclusions from carbonaceous chondrites: An experimental study. Ph. D. dissertation, the University of Chicago, Chicago Illinois, USA. 373 pp.

CAILLET C., MACPHERSON G. J. AND ZINNER E. K. (1993) Petrologic and Al-Mg isotopic clues to the accretion of two refractory inclusions onto the Leoville parent body: One was hot, the other wasn't. *Geochim. Cosmochim. Acta* **57**, 4725–4743.

CHEN J. H. AND WASSERBURG G. J. (1981) The isotopic composition of uranium and lead in Allende inclusions and meteoritic phosphates. *Earth Planet. Sci. Lett.* **52**, 1–15.

CONNOLLY H. C., JR. AND BURNETT D. S. (1999) Minor element distributions in spinels from type B CAIs: An experimental study (abstract). *Lunar Planet. Sci. Conf.* **30**, #1459, Lunar and Planetary Institute, Houston, Texas, USA (CD-ROM).

DAVIS A. M. AND MACPHERSON G. J. (1996) Thermal processing in the solar nebula: Constraints from refractory inclusions. In *Chondrules and the Protoplanetary Disk* (eds. R. H. Hewins, R. H. Jones, and E. R. D. Scott), pp. 71–76. Cambridge Univ. Press, Cambridge, U.K.

EL GORESY A., ARMSTRONG J. AND WASSERBURG G. J. (1985) Anatomy of an Allende coarse-grained inclusion. *Geochim. Cosmochim. Acta* **49**, 2433–2444.

GREENWOOD N. N. AND EARNSHAW A. (1985) *Chemistry of the Elements*. Pergamon Press, Oxford, U.K. 1542 pp.

GROSSMAN L. (1972) Condensation in the primitive solar nebula. *Geochim. Cosmochim. Acta* **36**, 597–619.

KENNEDY A. K., BECKETT J. R., EDWARD D. A. AND HUTCHEON I. D. (1997) Trace element disequilibria and magnesium isotope heterogeneity in 3655A: Evidence for a complex multi-stage evolution of a typical Allende type B1 CAI. *Geochim. Cosmochim. Acta* **61**, 1541–1561.

MACPHERSON G. J. AND DAVIS A. M. (1993) A petrologic and ion microprobe study of a Vigarano type B refractory inclusion: Evolution by multiple stages of alteration and melting. *Geochim. Cosmochim. Acta* **57**, 231–243.

MACPHERSON G. J., PAQUE J. M., STOLPER E. AND GROSSMAN L. (1984) The origin and significance of reverse zoning in melilite from Allende Type B inclusions. *J. Geol.* **92**, 289–305.

MACPHERSON G. J., WARK D. A. AND ARMSTRONG J. T. (1988) Primitive material surviving in chondrites: Refractory inclusions. In *Meteorites and the Early History of the Solar System* (eds. J. F. Kerridge and M. S. Matthews), pp. 746–807. Univ. Arizona Press, Tuscon, Arizona, USA.

MEEKER G. P. (1995) Constraints on formation process of two coarse-grained calcium-aluminum-rich inclusions: A study of mantles, islands and cores. *Meteoritics* **30**, 71–84.

MEEKER G. P., WASSERBURG G. J. AND ARMSTRONG J. T. (1983) Replacement textures in CAI and implications regarding planetary metamorphism. *Geochim. Cosmochim. Acta* **47**, 707–721.

MURRELL M. T. AND BURNETT D. S. (1987) Actinide chemistry in Allende Ca-Al-rich inclusions. *Geochim. Cosmochim. Acta* **51**, 985–999.

PAQUE J. M. (1990) Relict grains in a Ca-Al-rich inclusion from Allende (abstract). *Lunar Planet. Sci.* **21**, 932–933.

SIMON S. B., GROSSMAN L. AND DAVIS A. M. (1991) Fassaite composition trends during crystallization of Allende Type B refractory inclusion melts. *Geochim. Cosmochim. Acta* **55**, 2635–2655.

SIMON S. B., KUEHNER S. M., DAVIS A. M., GROSSMAN L., JOHNSON M. L. AND BURNETT D. S. (1994) Experimental studies of trace element

partitioning in Ca-Al-rich compositions: Anorthite and perovskite. *Geochim. Cosmochim. Acta* **58,** 1507–1508

STOLPER E. (1982) Crystallization sequence of Ca-Al-rich inclusions from Allende: An experimental study. *Geochim. Cosmochim. Acta* **46,** 2159–2180.

STOLPER E. AND PAQUE J. (1986) Crystallization sequences of Ca-Al-rich inclusions from Allende: The effects of cooling rate and maximum temperature. *Geochim. Cosmochim. Acta* **50,** 1785–1806.

WARK D. A. (1983) The Allende meteorite: Information from Ca-Cal-rich inclusions on the formation and early evolution of the solar system. Ph.D. thesis, University of Melbourne, Melbourne, Australia. 385 pp.

WARK D. A. (1997) Conditions for forming Ca-Al-rich inclusion rim layers: Preliminary experiments. In *Workshop on Parent-Body and Nebular Modification of Chondritic Materials* (eds. M. E. Zolensky, A. N. Krot and E. R. D. Scott), pp. 63–64. *LPI Tech. Report* **97-02,** Lunar and Planetary Institute, Houston, Texas, USA.

WASSON J. T. (1985) *Meteorites: Their Record of Early Solar-System History.* W. H. Freeman and Company, New York, New York, USA. 155 pp.

YONEDA S. AND GROSSMAN L. (1995) Condensation of CaO–MgO–Al_2O_3–SiO_2 liquids from cosmic gases. *Geochim. Cosmochim. Acta* **59,** 3413–3444.